J. Fluid Mech. (2010), *vol.* 652, *pp.* 333–372.
doi:10.1017/S0022112009994095

DNS of wavepacket evolution in a Blasius boundary layer

K. S. YEO†, X. ZHAO, Z. Y. WANG AND K. C. NG

Department of Mechanical Engineering, National University of Singapore, Singapore 117576

(Received 4 August 2008; revised 15 December 2009; accepted 19 December 2009)

This paper presents the direct numerical simulation (DNS) of wavepacket evolution and breakdown in a Blasius boundary layer. The study covers the physical, spectral and structural aspects of the whole transition process, whereas previous studies have tended to focus on issues of a more limited scope. The simulations are modelled after the experiments of Cohen, Breuer & Haritonidis (*J. Fluid Mech.*, vol. 225, 1991, p. 575). The disturbance wavepackets are initiated here by a u-velocity and a v-velocity delta pulse. They evolve through a quasi-linear growth stage, a subharmonic stage and a strongly nonlinear stage before breaking down into the nascent turbulent spots. Pulse-initiated wavepackets provide a plausible model for naturally occurring laminar–turbulent transition because they contain disturbances in a broadband of frequencies and wavenumbers, whose sum of interactions determines the spatio-temporal progress of the wavepackets. The early development of the wavepackets accords well with established linear results. The ensuing subharmonic evolution of the wavepackets appears to be underpinned by a critical-layer-based mechanism in which the x-phase speeds of the fundamental two-dimensional and dominant three-dimensional waves with compatible Squire wavenumbers are approximately matched. Spectral data over the bulk of the subharmonic stage demonstrate good consistency with the action of a phase-locked theory recently proposed by Wu, Stewart & Cowley (*J. Fluid Mech.*, vol. 590, 2007, p. 265), strongly suggesting that the latter may be the dominant mechanism in the broadband nonlinear evolution of wavepackets. The dominant two-dimensional and three-dimensional waves are observed to be spontaneously evolving towards triad resonance in the late subharmonic stage. The simulations reproduce many key features in the experiments of Cohen *et al.* (1991) and Medeiros & Gaster (*J. Fluid Mech.*, vol. 399, 1999*b*, p. 301). A plausible explanation is also offered for the apparently 'deterministic' subharmonic behaviour of wavepackets observed by Medeiros & Gaster. The strongly nonlinear stage is signified by the appearance of low-frequency streamwise-aligned u-velocity structures at twice the spanwise wavenumber of the dominant three-dimensional waves, distortion of the local base flow by the strengthening primary Λ-vortex and rapid expansion of the spanwise wavenumber (β) spectrum. These are in broad agreement with the experimental observations of Breuer, Cohen & Haritonidis (*J. Fluid Mech.*, vol. 340, 1997, p. 395). The breakdown into incipient turbulent spots occurs at locations consistent with the experiments of Cohen *et al.* (1991). A visualization shows that the evolving wavepackets comprise very thin overlapping vorticity sheets of alternating signs, in stacks of two or three. Strong streamwise stretching of the flow at the centre of the wavepacket in the late subharmonic and strongly nonlinear stages promotes the roll-up and intensification of the vorticity sheets into longitudinal vortices, whose mutual induction precedes the

† Email address for correspondence: mpeyeoks@nus.edu.sg

breakdown of the wavepacket. The critical layer of the dominant two-dimensional and oblique wave modes reveals the progressive coalescence of a strong pair of vortices (associated with the Λ-vortex) during the subharmonic stage. Their coalescence culminates in a strong upward burst of velocity that transports lower momentum fluid from below the critical layer into the upper boundary layer to form a high shear layer in the post-subharmonic stage.

1. Introduction

The boundary layer is a very critical region of a flow past a solid body. The state of the boundary layer, whether laminar or turbulent, directly affects the skin friction and heat transfer from the surface and the onset of flow separation under adverse pressure conditions and so on. A vast body of knowledge has been gained in the last four decades of the complex process of transition from laminar to turbulent state. This knowledge pertains largely to the behaviour of regular wave systems under laboratory conditions. The behaviour of more complex disturbances such as those of wavepackets encountered in natural transition is less well understood. A comprehensive knowledge of the latter will aid formulation of measures to delay or slow down the process of transition and realize the benefits of laminar flow.

There are two main classes of transition in a boundary layer according to Morkovin (1969). The first is the traditional Tollmien–Schlichting (TS) wave route whereby, having been excited by a suitable receptivity mechanism, the disturbance waves first grow linearly as TS waves. This is followed by nonlinear wave interactions, when the waves have acquired sufficient size, and then final breakdown to turbulence. The second class is bypass transition, whereby the large initial amplitude of the disturbance allows it to go into the nonlinear breakdown stage directly and proceed to turbulence from there. Nevertheless, it is the linear mechanism that ultimately drives disturbance growth (Reddy & Henningson 1993) – derivation of the Reynolds–Orr equation shows that the nonlinear terms play no direct role in extracting energy from the mean flow, although they play a role in redistributing energy among the wave modes. Bypass transition has attracted considerable interest in recent years (see Schmid & Henningson 2000 for a thorough review). However, in this study, we are concerned primarily with transition initiated by small disturbances.

Our most comprehensive knowledge of the process of boundary-layer transitions has been derived from system experiments with regular harmonic plane waves. For two-dimensional TS waves with relatively large initial amplitude that exceeds 1 % of the free-stream velocity, the waves evolve into a series of aligned Λ-shaped three-dimensional structures that have the same frequency as the fundamental two-dimensional wave. When the initial amplitude is small, the two-dimensional TS harmonic wavetrain may grow linearly for a considerable distance before it also develops into a series of Λ-shaped disturbance structures. These structures have a staggered formation and a frequency that is about half the frequency (subharmonic) of the two-dimensional TS waves. Once formed, the three-dimensional structures or waves amplify rapidly to overtake the primary two-dimensional wave, so that the disturbance wave field becomes effectively three-dimensional in a relatively short distance. The large three-dimensional wave disturbances in turn distort the local mean velocity profile, resulting in instantaneous profile inflexions and the formation of high-shear layers. A rapid proliferation of higher wave harmonics precedes the

breakdown to a chaotic or turbulent flow state. The two sequences of wave development and breakdown are termed the K-type breakdown and subharmonic breakdown, respectively. The subharmonic breakdown is also frequently termed the C- or H-breakdown. The 'C' refers to Craik (1971), who proposed a theory based on resonant interaction between the fundamental two-dimensional and a symmetric pair of oblique waves to explain the appearance of subharmonic three-dimensional wave structures in boundary layers. The 'H' refers to Herbert (1983), who subsequently proposed a more generalized model of secondary instability to explain the appearance of the subharmonic modes in boundary layers, as well as the appearance of such structures in plane channel flow, where Craik's model is inapplicable. In Herbert's theory, the development of subharmonic waves with wavelengths twice the fundamental two-dimensional wavelength originates from principal parametric resonance between the fundamental two-dimensional TS wave of finite amplitude A_{2D} and the oblique wave pair. Herbert's model approximates the Craik's model in the limit of small A_{2D}. A review of the experimental and theoretical background can be found in Kachanov (1994) and Herbert (1988), respectively.

The theories and experiments for regular harmonic waves could not reproduce the intermittence and spotty structures of naturally occurring turbulence. Natural transition occurs in an environment in which the initiating disturbances are typically non-homogeneous in space and time. Pulse-induced disturbances, which contain a broad spectrum of wavenumbers and frequencies, are generally regarded as a better representative of the disturbance sources for the study of natural transition process (see Medeiros & Gaster 1999*a*). However, the broad spectrum of waves present also poses considerable challenges in terms of modelling and analysis.

Vasudeva (1967) was probably the first to experiment with pulse-initiated wavepackets in a transition study. However, he was unable to get satisfactory results because of poor signal-to-noise problems. Gaster & Grant (1975) successfully studied the evolution of wavepackets in a laminar boundary layer by applying an ensemble-averaging technique to overcome the signal/noise problem. Furthermore, Gaster (1975) presented a theoretical model of wavepacket evolution based on numerical Fourier wave techniques. Both these studies concern the linear growth of wavepackets before the onset of significant wave nonlinearity.

Cohen, Breuer & Haritonidis (1991) extended the experimental work done by Gaster & Grant (1975) to cover the entire transition process of the wavepacket from the linear growth stage through to the formation of the incipient turbulent spot. In their experiments, the wavepackets were initiated by air pulses comprising a single period of a 24 Hz sinusoid. The linear stage agreed very well with the measurements of Gaster & Grant (1975). This was followed by a weakly nonlinear stage that was characterized by the growth of oblique subharmonic waves whose frequencies were about half that of the most-amplified two-dimensional TS waves. In a critical comparison with linear stability theory, Cohen (1994) found that these waves started to grow nonlinearly well ahead of the branch II neutral point of the fundamental wave. Breuer, Cohen & Haritonidis (1997) subsequently carried out a more detailed investigation of the strongly nonlinear stage and the breakdown of the wavepacket into a turbulent spot. They found that the strongly nonlinear growth stage was characterized by low-frequency waves with growing amplitudes, oblique waves with increasing spanwise wavenumbers and higher harmonic waves with relatively lower amplitudes. They also reported that the formation stage of the turbulent spot began with the growth of high-frequency waves proceeding from the sums and differences of fundamental and three-dimensional waves. A rapidly expanding cascade of waves

and a loss of phase coherency that is indicative of a chaotic state precipitate the final turbulent spot.

The process of subharmonic growth in wavepackets in a boundary layer was the focus of Medeiros & Gaster (1999*a*). They concluded that the phase content of the initial wavepacket could have a deterministic influence on the nonlinear three-dimensional development of the wavepacket. Earlier, Shaikh & Gaster (1994) and Shaikh (1997) had studied the transition caused by a point source generating white noise as a model of natural transition. Similar to the wavepacket findings of Breuer *et al.* (1997), the late nonlinear stage was characterized by the dominance of low-frequency waves and localized bursts of high-frequency waves preceded the formation of turbulent spots. However, the complexity of the continuous wave stream prevents more detailed physical features of the breakdown process from being extracted.

On the whole, there have been fairly limited numerical studies conducted on the transition of wavepackets in boundary layers. The early numerical transition studies, such as Fasel (1976) and Spalart & Yang (1987), were concerned with two-dimensional harmonic wavetrains or resonating triads of harmonic waves. The first numerical simulation of wavepacket evolution in a spatially developing Blasius boundary layer was probably presented by Konzelmann & Fasel (1991). The simulation, which covered the linear and early subharmonic growth stages, exhibits contour envelopes of the wavepackets that are generally in good agreement with the experiments of Gaster & Grant (1975), although the amplitudes in the simulations are larger than those in the experiments. Bech, Henningson & Henkes (1998) carried out a comparative study of the linear and nonlinear growth behaviour of localized disturbances in zero- and adverse-pressure-gradient boundary layers. The spatially growing boundary layers were approximated as temporally growing parallel shear flows by the artificial inclusion of a body force in the mean-flow equation. They found that secondary instability plays a less significant role in the nonlinear wave development for the adverse pressure gradient cases due to the rapid growth of primary two-dimensional waves.

Henningson, Lundbladh & Johansson (1993) studied bypass transition from localized disturbances in wall shear flows. The behaviour of turbulent spots in plane Poiseuille and boundary layer flows was studied by Henningson, Spalart & Kim (1987). The mature turbulent spot in the boundary layer has the appearance of an arrowhead pointing in the stream direction, which is in agreement with the experiments of Cantwell, Coles & Dimotakis (1978) and other researchers, whereas the arrowhead-shaped turbulent spot in the Poiseuille flow points upstream. Singer (1996) conducted the detailed simulation of turbulent spot behaviour in a boundary layer. The turbulent spots in these studies were produced from strong localized disturbances that effectively bypassed the linear and earlier nonlinear stages. Jacobs & Durbin (2001) simulated boundary layer turbulent spots in a bypass-type transition numerically.

Wavepacket simulation in boundary layers, as noted above, has hitherto been largely focused on selective aspects of the transition process rather than on the whole transition process from small seeded disturbances to final breakdown. Thus, large initial disturbance amplitudes have frequently been used in studying the nonlinear breakdown stage to reduce the evolution distance and time, while parallel-flow-type approximation (using body force) has been applied in some cases to render the problem periodic in the stream direction. These had been necessary to render the size of the numerical problem within the means of the then available computational resources. However, with continuous advances being made in computing speed, the

advent of highly parallelized computing and the greatly reduced cost of memory and data storage, computationally intensive simulation of wavepackets evolving in a spatially extended boundary layer has become feasible.

This paper is concerned with a numerical study of the process of laminar–turbulent transition of pulse-initiated wavepackets in a spatially growing Blasius boundary layer. The simulation follows the evolution of an initially small disturbance wavepacket from its pulsed inception, through the linear growth stage, the nonlinear secondary instability stages and its final nonlinear breakdown into an incipient turbulent spot. The simulation follows closely the conditions of Cohen *et al.*'s (1991) experiments, which cover the whole transition process. Numerical simulation is able to provide spatial details of the evolving wavepackets that could not be ascertained from experiments and offers a comprehensive picture of the spectral and structural evolution of the developing wavepackets leading up to the formation of the incipient turbulent spot. Pulsed-induced wavepacket is the focus of the study because it presents a good model for the type of broadband disturbances that one may encounter in a natural transition scenario. The broadband character of a wavepacket offers a central advantage in permitting natural selection of most dominant waves to operate through the sum of its growth processes. This may be helpful in identifying the critical waves and key processes that are involved at the various stages in natural transition. This study was conducted to support related investigations into the behaviour of disturbance wavepackets evolving over flexible panel arrays, where the effects of the flexible arrays on the various stages of evolution and their cumulative consequences on turbulent spot formation are examined. These will be reported in the future.

2. Numerical simulation

2.1. *Numerical scheme*

The numerical simulation is carried out by the direct numerical simulation (DNS) code developed by Wang (2003) and Wang, Yeo & Khoo (2005) for the incompressible Navier–Stokes equations:

$$\frac{\partial u_i}{\partial x_i} = 0, \tag{2.1}$$

$$\frac{\partial u_k}{\partial t} + \frac{\partial}{\partial x_i}(c_2\bar{u}_i u_k + c_2 u_i \bar{u}_k + c_1 u_i u_k) = \frac{\partial}{\partial x_i}\left(\frac{1}{Re}\frac{\partial u_k}{\partial x_i}\right) - \frac{\partial p}{\partial x_k}, \tag{2.2}$$

where $i, k = 1, 2, 3$ denote the streamwise (x), the wall normal (y) and spanwise (z) coordinates of the Cartesian frame respectively. The perturbation form of the Navier–Stokes equations (2.1) and (2.2) is obtained by setting $c_1 = c_2 = 1.0$, where $\bar{u}_i$ denote the components of the base flow. Time integration of the Navier–Stokes equations is accomplished by a fully implicit fractional-step algorithm, in which the divergence-free condition is maintained by a pressure-correction procedure. Spatial discretization is based on coordinate-transformed curvilinear finite volume with second-order flux evaluation. Detailed resolution of the near-wall flow is achieved by grid stretching. The implicit iterative implementation ensures there is good numerical stability without artificially introduced dissipation. The overall numerical scheme is second-order accurate in space and time. More details concerning the scheme and grid may be found in the cited references. The base flow used in the present study is the non-parallel Blasius boundary layer. The Reynolds number Re is based on the free-stream velocity U_∞, the displacement thickness δ_0 of the boundary layer at the reference location where the disturbance pulse is introduced and the kinematic

viscosity of the fluid. The code has been extensively validated against published linear and nonlinear wave results of Fasel, Rist & Konzelmann (1990) and Liu & Liu (1994) in Wang *et al.* (2005), who carried out a comparative study of the evolution and breakdown of harmonic wave triads over rigid and compliant membrane surfaces. The non-perturbation version of the code has also been applied in the DNS study of low-Reynolds-number turbulent channel flows over dimple arrays in Wang *et al.* (2006).

2.2. *Simulation of experimental conditions*

The computational set-up closely emulates the experimental conditions of Cohen *et al.* (1991). The computational domain spans $310 \leqslant X \leqslant 1510$ in the streamwise direction (corresponding to $0.72\ \mathrm{m} \leqslant x \leqslant 3.5\ \mathrm{m}$ in the experiments), $0 \leqslant Y \leqslant 54$ ($0.0\ \mathrm{m} \leqslant y \leqslant 0.25\ \mathrm{m}$) in the wall normal direction and $-172 \leqslant Z \leqslant 172$ ($-0.4\ \mathrm{m} \leqslant z \leqslant 0.4\ \mathrm{m}$) in the spanwise direction. The (X, Y, Z) denotes the non-dimensional Cartesian coordinates based on the reference length $\delta_0 = 2.3182 \times 10^{-3}\ \mathrm{m}$, which is the displacement thickness of the boundary layer at the location $X_0 = 349.4$, where the disturbance is introduced (corresponding to $x_0 = 0.81\ \mathrm{m}$ for the same in the experiments). The free-stream velocity is $U_\infty = 6.65\ \mathrm{m\,s^{-1}}$ and the kinematic viscosity is $\upsilon = 1.49 \times 10^{-5}\ \mathrm{m^2\,s^{-1}}$. The Reynolds number $Re_\delta = \delta U_\infty/\upsilon$ at the excitation source is 1034.6.

The initiating disturbance in Cohen *et al.*'s (1991) experiments was an air pulse introduced at the wall via a perforated disk of 0.5 cm diameter (X-diameter = 2.16). The pulse of air was sustained over a single period of a 24 Hz sinusoid ($F = 10^6\omega_\delta/R_\delta = 50.8$). Cohen *et al.* (1991) performed two sets of transition studies using two different initiating source amplitudes. For the first or small-amplitude case, the disturbance $|u|_{max}$ measured about 0.3 % at height $y/\delta = 0.62$ when the wavepacket passed the first measurement station at $x = 160$ cm (corresponding to $X = 690$ here). The large-amplitude case had $|u|_{max} \approx 0.6\,\%$ at $x = 170$ cm ($X = 733$). They are designated as the S case and L case, respectively, for the ease of reference in this paper. Owing to the small size of the experimental disturbance source, a delta or point-velocity pulse having the same time modulation as the experiments is used to initiate the wavepackets in the present simulation. Two cases are simulated here. The initiating source is a u-velocity pulse applied at $X_0 = 349.4$ on the wall in the first case (termed the u-initiated case) and a v-velocity pulse in the second (the v-initiated case). The two different modes of initiation are selected for the purpose of assessing if the mode of initiation would make a significant difference to the overall evolution and breakdown of the wavepacket. For both cases, the disturbance $|u|_{max} \approx 0.4\,\%$ when the wavepacket arrives at $X = 690$ – this is intermediate in size between the S and L cases of Cohen *et al* (1991).

A computational simulation is carried out in terms of the global length scale δ_0. The non-dimensional simulation time $T = tU_\infty/\delta_0$ is measured from the time of pulse initiation. The frequency ω and the wavenumber (α, β) in the global/computational length scale are related to the corresponding quantities in the local displacement thickness length scale $\delta(x)$ by

$$\omega_\delta = \omega(X/X_0)^{1/2} = \omega(x/x_0)^{1/2}, \tag{2.3a}$$

$$(\alpha, \beta)_\delta = (\alpha, \beta)(X/X_0)^{1/2} = (\alpha, \beta)(x/x_0)^{1/2}, \tag{2.3b}$$

where the subscript δ denotes quantities in the local length scale $\delta(x)$.

Equations (2.1) and (2.2) govern the temporal–spatial evolution of the disturbance velocity field $(u_i) = (u, v, w)$, which is assumed to have been duly non-dimensionalized.

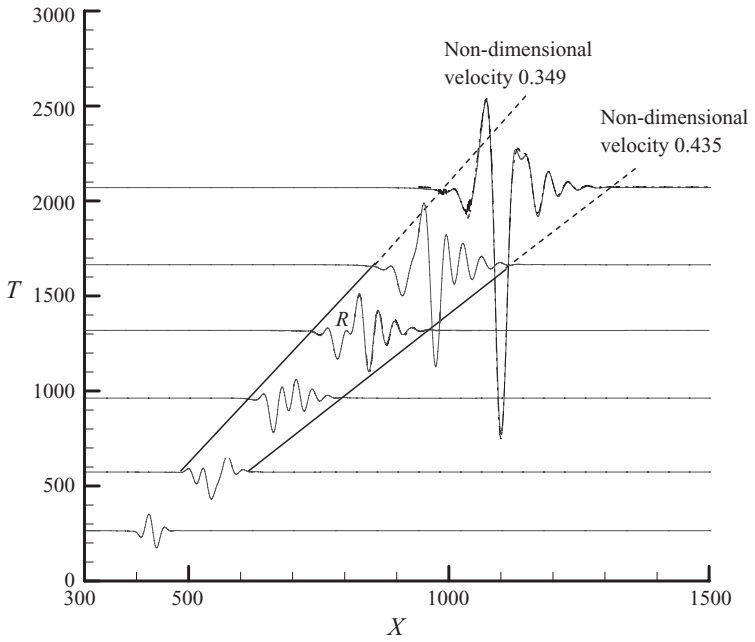

FIGURE 1. Disturbance wavepackets (u-initiated pulse) along the centreline ($z = 0$) at height $y/\delta \approx 0.62$ for different times, where δ denotes the local displacement thickness. Solid lines are for grid $1170 \times 47 \times 81$. Dot-dashed lines are for grids $1170 \times 47 \times 163$ at $T = 1310$ and $1170 \times 65 \times 163$ at $T = 2046$. R denotes ripple.

The disturbance velocity components are assumed to be zero at the inflow boundary of the computational domain. The disturbance velocity was also approximated to be zero at the top boundary, which is set at eight to ten boundary layer thicknesses away from the wall. Centreline symmetry is not assumed here for the disturbance. Periodic boundary conditions are imposed on the two side boundaries. This allows non-symmetric disturbance modes, if any, to develop freely. A buffer domain (Liu & Liu 1994) was instituted at the outflow boundary to allow the disturbances to pass out of the computational domain without upstream reflection.

2.3. *Computational grid*

The disturbance wavepackets are simulated on a (x, y, z)-grid of $1170 \times 47 \times 81$ for the linear and early nonlinear growth stages. The disturbance field data are then spline-interpolated onto a finer cross-sectional grid with 65×163 (y, z)-grid points for the remaining simulation until the first appearance of the incipient turbulent spot. The grid is uniform in both the streamwise and spanwise directions. The grid in the wall-normal or y-direction is geometrically stretched to give good resolution to the finer flow details near the wall. Similar stretched grids have been used by Wang *et al.* (2005) in their study of wave breakdown. Das & Matthew (2001) also emphasized the application of grid stretching to resolve unstable wave structures in their DNS study of disturbance waves and turbulent spots. The finer cross-sectional grid is introduced to ensure that the smaller-scale structures that develop during the later stages of transition are adequately resolved.

Figure 1 shows the spatial–temporal development of the u-velocity component of the u-initiated wavepacket along the centreline $z = 0$ at the height of $y/\delta = 0.62$. The results at the non-dimensional time $T = 1310$ compare the wave in the very early

nonlinear stage ($|u|_{max} \approx 0.6\,\%$) with a similar wave computed with twice the number of grid intervals in the spanwise direction. The solid line shows the streamwise disturbance based on the original grid of $1170 \times 47 \times 81$, while the dot-dashed line shows the results on the finer grid. The two waves are almost identical in their details. The solution on the initial lower-resolution 47×81 (y, z)-grid was next interpolated onto a refined 65×163 (y, z)-grid and simulation was carried out on the refined grid thereafter. The results from the original and refined grids at the subsequent time of $T = 2046$ are compared in figure 1. The waves are in their mid-nonlinear growth phase at this time (with a clearly defined Λ-vortex and $|u|_{max} \approx 3.4\,\%$; see later results). The very small differences in the two waves indicate that the original lower-resolution grid should be adequate up to the mid-nonlinear stage at least. We note that the very small differences could also be contributed by numerical errors introduced during grid interpolation. These small differences can have no significant effects on the dynamics and process of wavepacket evolution and breakdown, which is governed by much larger-scale processes at this stage. The x-grid of 1170 was found to be generally adequate throughout in capturing the wave details. Grid studies show that the finer (y, z)-grid is able to capture the breakdown process in all its essential details. In this regard, adequate spanwise resolution was found to be particularly crucial for capturing the rapidly expanding spanwise wavenumber (β) spectrum during the late nonlinear stage, just prior to the final breakdown.

The final breakdown process exhibits typical traits of a dynamical system entering a state of chaos, whereby all perturbations or errors are rapidly amplified. Nevertheless, the apparent disorder is governed by certain generic (robust) dynamics on an inertial submanifold of low dimension in phase space, and the properties of such a system may frequently be characterized in statistical and spectral terms. In this study, the finer grid was found to make a notable difference only during the brief moments of wavepacket breakdown, as signified by a burst of fine structures – here the rates may be slightly enhanced. An extensive discussion of dynamical system issues in fluid dynamics and turbulence, including aspects concerning its approximation and numerical simulation, is given by Holmes, Lumley & Berkooz (1996).

3. Results and discussions

In this section, we present a comprehensive numerical study of the continuous transition process of the wavepackets from their pulsed inception to their breakdown into the incipient turbulent spots. The physical, spectral and vortical aspects of the evolution process are examined.

3.1. *Analysis of spatial evolution*

Figures 1 and 2 show the streamwise (u-) velocity component along the centreline ($z = 0$) of the disturbance wavepacket (u-initiated case) at different time stages. From figure 1, it can be seen that the leading and trailing edges of the wavepacket travel at speeds of about $0.435U_\infty$ and $0.349U_\infty$, respectively, during the linear and early nonlinear evolving stages. These are close to the values of $0.44U_\infty$ and $0.36U_\infty$ obtained by Gaster (1975) from Fourier synthesis of Orr–Sommerfeld solutions. The disturbance pulse was initiated at $Re = 851$ by Gaster (1975) whereas the present wavepacket is initiated at $Re_\delta \approx 1000$.

Figure 1 shows that the wavepacket is composed of two wave cycles at the early time of $T = 260$. With differential leading and trailing edge speeds, it expands spatially to about five wave cycles by time $T = 930$. The wavepacket develops very much in

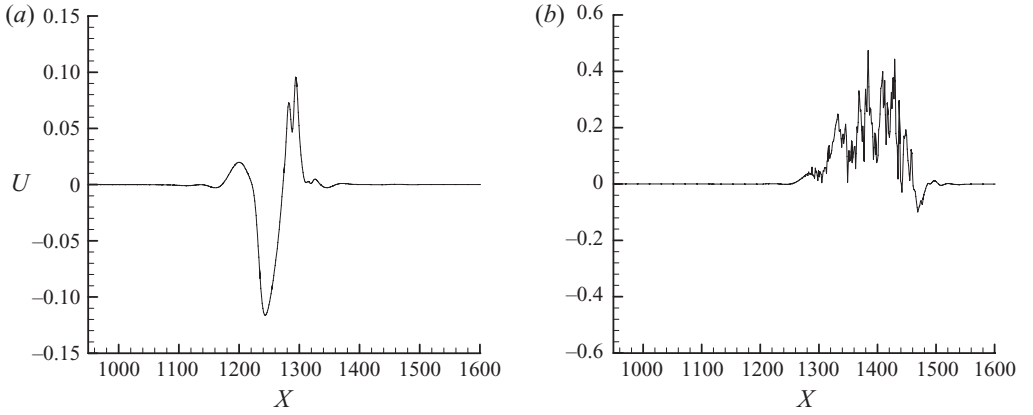

FIGURE 2. Disturbance wavepackets (u-initiated pulse) along the centreline at $y/\delta \approx 0.62$ for times (a) $T = 2417$, (b) $T = 2674$. Grid $1170 \times 65 \times 163$.

accordance with the experimental and theoretical results of Gaster & Grant (1975) and Gaster (1975) until $T = 1280$, where the disturbance wave amplitude just crosses the 0.5 % mark. The first sign of wave distortion appears at about $T = 1310$, taking the form of a small ripple (denoted by R) in the second wave cycle, leading thence to the formation of a large negative velocity 'spike' near the start of the third wave cycle at $T = 1660$. As we shall see below, this is associated with the beginning of a secondary or nonlinear wave instability. The negative velocity 'spike' is amplified considerably by time $T = 2046$ and continues to be an important feature of the disturbance wavepacket until its breakdown. Subsequent time stages of the greatly amplified wavepacket at $T = 2417$ and 2674 are shown in figure 2. Higher wave harmonics are evident at $T = 2417$, although the wave structures remain essentially smooth at this time. Higher harmonic waves have also developed spanwise within the wavepacket. A catastrophic change to the wavepacket follows. This is marked by the very rapid breakdown of the wavepacket into a burst of small-scale high-frequency high-amplitude fluctuations (the incipient turbulent spot) within a distance that is less than the streamwise size of the disturbance wavepacket by the time $T = 2674$ in figure 2(b).

A more detailed depiction of the evolution and breakdown of the u-initiated wavepacket is presented in figure 3. This figure shows the u-velocity component of the disturbance wavepacket at the height of $y/\delta \approx 0.62$, which is the height at which wave measurements were made in the experiments of Cohen *et al.* (1991) and Medeiros & Gaster (1999*b*). It also corresponds to the height where the dominant u-component of disturbance fluctuations is generally the largest for both two-dimensional and three-dimensional waves according to linear stability theory. The contours indicate that the early u-initiated wavepacket at $T = 260$ (figure 3a) has distinct maximum and minimum of u along the centreline, which is consistent with its two-dimensional depiction in figure 1. From there, the wavepacket evolves into the customary crescent shape and $|u|_{max}$ decays to about 0.4 % when the wavepacket arrives at $X \approx 690$ in figure 3(b) (which corresponds to the first measurement station in Cohen *et al.* (1991) at $x = 160$ cm). The location of the wavepacket is indicated here by the x-position of its approximate centre. The u-velocity maxima on both sides of the centreline reflects the rapidly growing dominance of the oblique waves over the two-dimensional waves. The shape of the wavepacket is similar to that of Gaster & Grant (1975), although

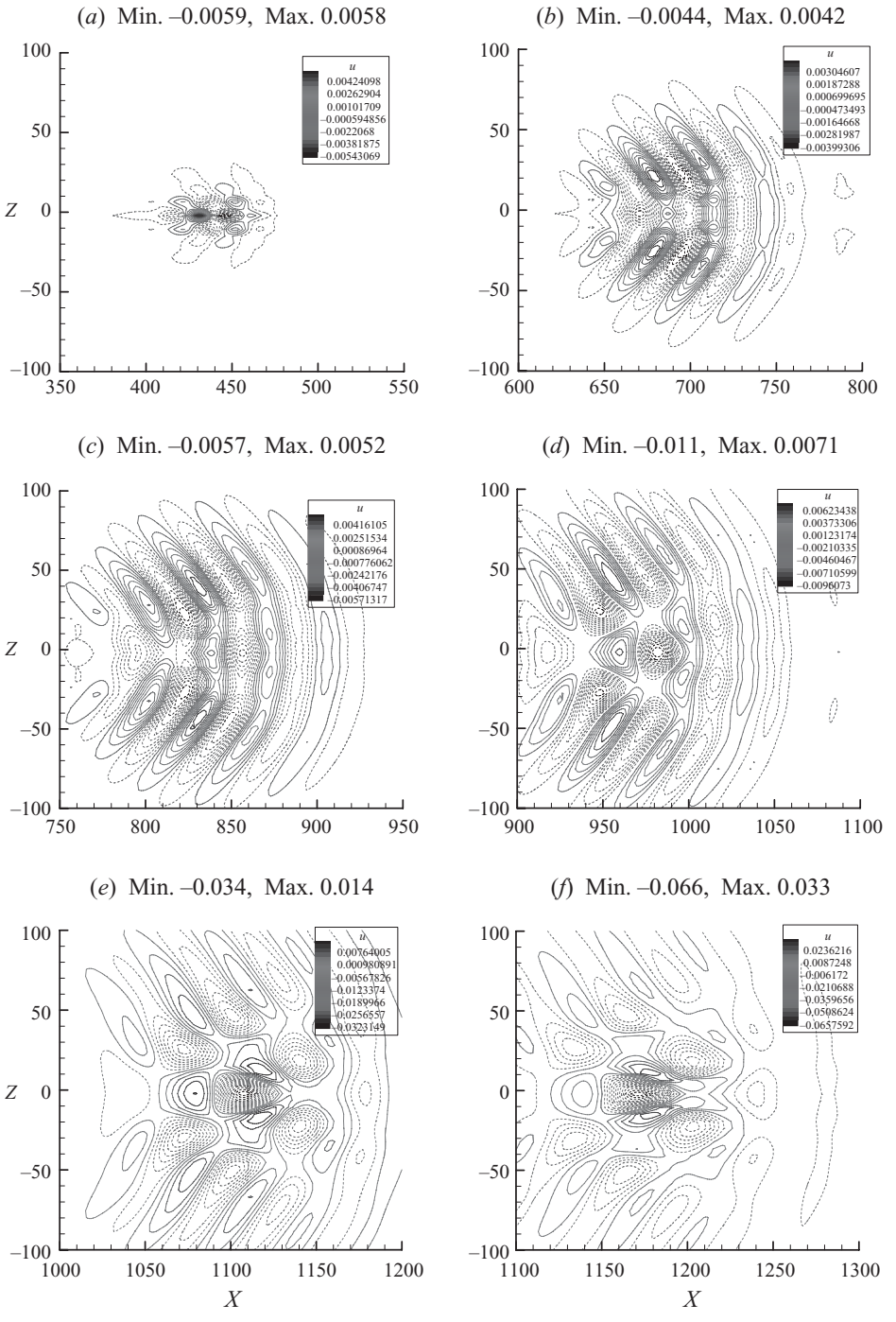

FIGURE 3(*a–f*). For caption see facing page.

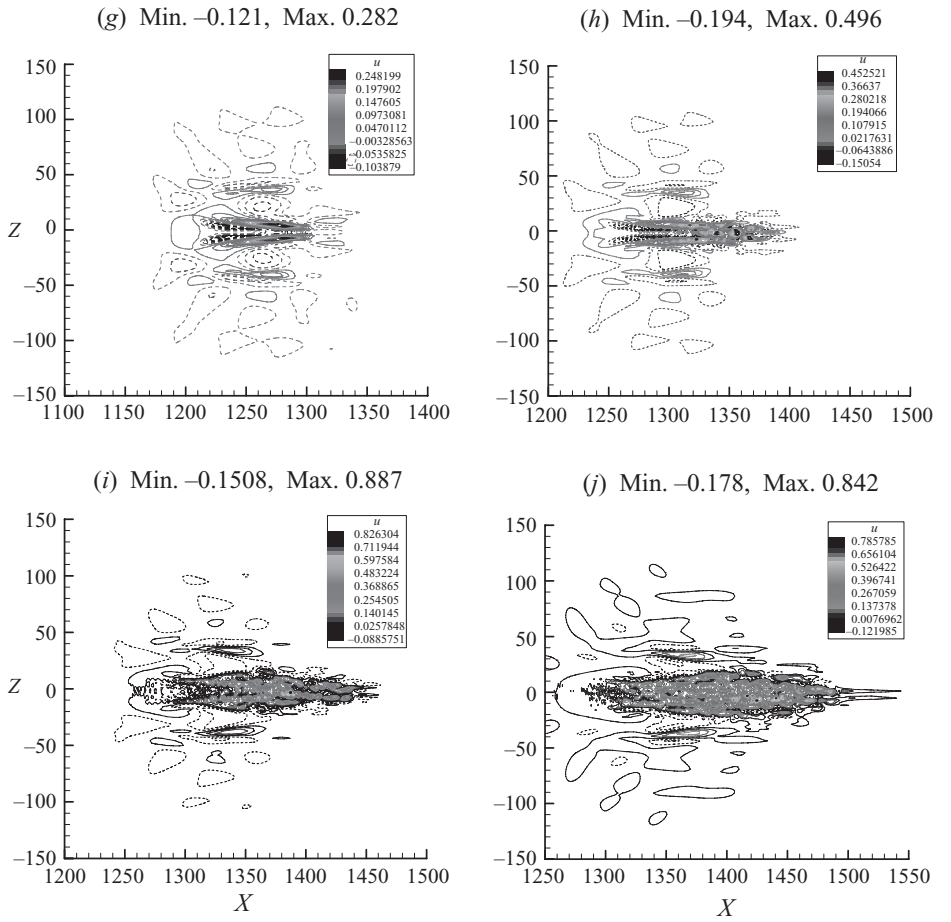

FIGURE 3. Contours of disturbance streamwise velocity u for u-initiated wavepacket at $y/\delta \approx 0.62$ at times: (*a*) $T = 260$; (*b*) $T = 930$; (*c*) $T = 1310$; (*d*) $T = 1670$; (*e*) $T = 2046$; (*f*) $T = 2231$; (*g*) $T = 2417$; (*h*) $T = 2528$; (*i*) $T = 2600$; (*j*) $T = 2674$. Solid lines represent positive contours and dotted lines represent negative contours. Minimum (Min.) and maximum (Max.) contour values are indicated.

the latter results pertain to measurements and computations at points outside the boundary layer, where disturbance structures tend to be smoother. The wavepacket is into the early subharmonic stage in figure 3(*c*) ($X \approx 850$) where its $|u|_{max} \approx 0.57\,\%$. Figure 3(*d*,*e*) shows the evolution of the wavepacket through the weakly nonlinear subharmonic stage leading up to the formation of a distinctive Λ-shaped structure at its centre. During this stage, $|u|_{max}$ rises to 6.6 % of U_∞ in figure 3(*f*) ($X \approx 1170$). Weaker Λ-shaped structures in staggered formation may also be broadly observed in figure 3(*e*,*f*). Figure 3(*f*,*g*) spans the strongly nonlinear post-subharmonic stage, where the subharmonic waves gain more energy and their amplitudes increase rapidly. Here the dominant Λ-shaped structure (Λ-vortex) at the centre of the wavepacket warps downstream to form two narrow streamwise velocity streaks in figure 3(*g*) ($X \approx 1260$). The concentration of negative and positive u-contours defining the two streaks points to strong streamwise stretching of the flow within the streaks. From here, the wave structures begin to lose their symmetry and regularity (figure 3*h*). The loss of symmetry emanates at the front of the stretched Λ-vortex. The wavepacket

breaks down into an apparent cluster of smaller-scale structures in figure 3(*i,j*). The weaker outlying waves nevertheless remain highly symmetrical however. The loss of symmetry may be induced by numerical noise or modelling imperfections. The loss of structural regularity/smoothness and ensuing breakdown into the nascent turbulent spot (figure 3*h,i*) occurs within a very short distance of $\Delta X \approx 50$ and time interval of $\Delta T \approx 100$, which are about 5 % and 4 % of the total evolution distance and time of the wavepacket from its initiation, respectively. The incipient turbulent spot in figure 3(*i,j*) has a spindle-shaped turbulent core comprising disturbance structures in a wide range of streamwise length scales. The turbulent core is fringed on both sides by streamwise-aligned wavelets superimposed on weak oblique remnants of the crescent waves (see figure 5*c*). Overall, the incipient spot is shaped like an arrowhead pointing in the direction of the flow (Cantwell *et al.* 1978; Henningson *et al.* 1987).

Figure 4 shows selected snapshots of the *u*-velocity contours for the corresponding *v*-initiated wavepacket for comparison. The early *v*-initiated wavepacket at time $T = 260$ in figure 4(*a*) differs from the early *u*-initiated wavepacket in figure 3(*a*). The occurrences of u_{max} are found in two distinct symmetrically paired *u*-velocity jets at the centre of the wavepacket, whereas the u_{max} occurs on the centreline in the rear half of the *u*-initiated packet. Despite these initial differences, the *v*-initiated wavepacket evolves to look very similar to the corresponding *u*-initiated wavepacket by $T = 930$ in figure 4(*b*) ($X \approx 690$), except for the presence of a very weak frontal streak. The two wavepackets have comparable $|u|_{max} \approx 0.4\,\%$ and are close to the threshold of the secondary instability stage. The growth of the wavepacket through the secondary instability stage and the formation of Λ-shaped structures captured in figure 4(*c,d*) match closely those for the *u*-initiated wavepacket in figure 3(*c–f*), except in the details. Note the close similarity of the figures at times $T = 1310$ (figures 3*c* and 4*c*) and $T = 2046$ (figures 3*e* and 4*d*) in terms of both their disturbance magnitudes and contour distributions. Finally, figure 4(*e*) shows the two strong streamwise velocity streaks that emerge from the two arms of the Λ-structure (vortex) at time $T = 2417$. The nascent turbulent spot appears to form by $T \approx 2600$ at a position that is marginally ahead of that for the *u*-initiated spot. It is not possible for one to be exact about the time and location for the appearance of the nascent spot since there is no precise criterion defining one. This shows that while the initial phase contents of wavepackets with similar $|u|_{max}$ do have some effects on their transition details (see Shaikh & Gaster 1994), the effects appear to be quite small considering the substantial distances the two wavepackets had travelled from their initiation point. For discussion purposes, we could regard the two wavepackets as having approximately the same transition location and time.

We recall that the experiments of Cohen *et al.* (1991) were conducted for two initial amplitudes: a small initial amplitude case with $|u|_{max} \approx 0.3\,\%$ at $x = 160$ cm and a larger initial amplitude case with $|u|_{max} \approx 0.6\,\%$ at $x = 170$ cm (called the S case and L case, respectively). Both underwent the same transition stages, except in so far as the stages were brought forward in both space and time for the L case. In the L case, the wavepacket was plunged immediately into the secondary instability stage, largely bypassing the linear growth stage.

Cohen *et al.* (1991) placed the occurrence of the turbulent spots for the S and L wavepackets at $x \approx 350$ cm and 270 cm, respectively. The onset of turbulent spots in the experiments was ascertained by a major loss of coherence in the ensemble averaging of the disturbance signals rather than by direct visualization of the disturbance structures. From figure 3(*h–j*), one may locate the corresponding onset of the turbulent spot for the present simulated wavepackets at around $X \approx 1350$ (or $x \approx 310$ cm). The value

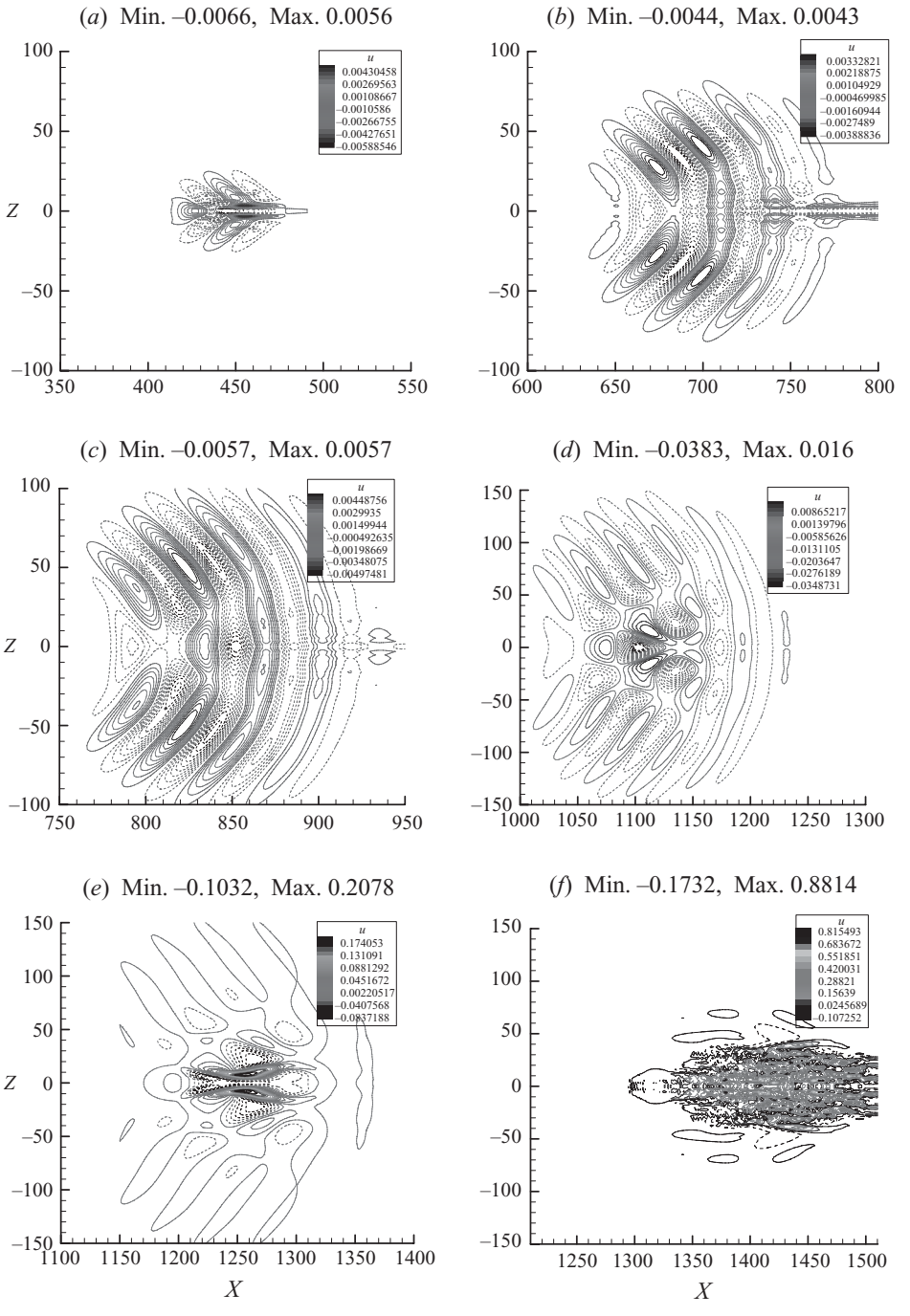

FIGURE 4. Contours of disturbance streamwise velocity u for v-initiated wavepacket at $y/\delta \approx 0.62$ at times: (*a*) $T = 260$; (*b*) $T = 930$; (*c*) $T = 1310$; (*d*) $T = 2046$; (*e*) $T = 2417$; (*f*) $T = 2788$. Solid lines represent positive contours and dotted lines represent negative contours. Minimum and maximum contour values are indicated.

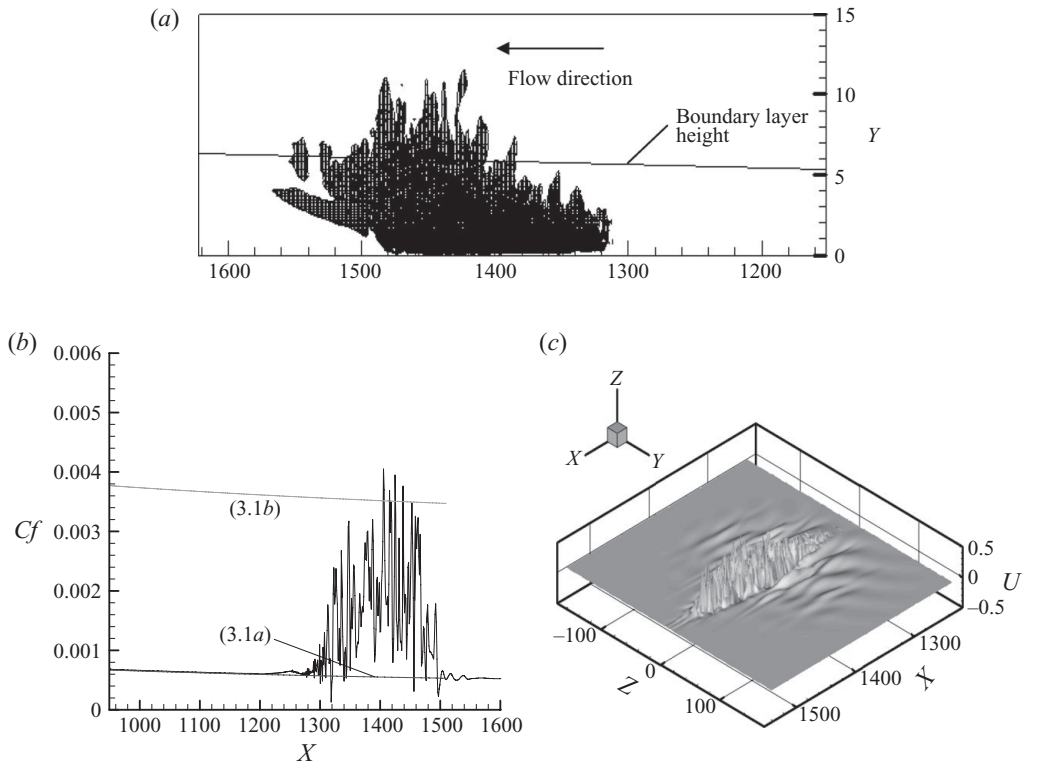

FIGURE 5. Incipient turbulent spot at $T = 2674$. (a) Instantaneous side profile view based on u-velocity fluctuations. (b) Instantaneous local skin friction coefficient along the centreline ———: the bottom line for laminar boundary layer based on (3.1a) and the top line for fully developed turbulent boundary layer based on (3.1b). (c) Perspective view of u-velocity fluctuations at height $y/\delta \approx 0.62$.

is right between the onset locations for the S and L cases. Because the simulated wavepackets have an intermediate disturbance amplitude of $|u|_{max} \approx 0.4\,\%$ between the two cases, there is clearly good consistency between the present simulation and the experiments of Cohen *et al.* (1991) as far as the position for the occurrence of the turbulent spot is concerned.

The present u- and v-initiated wavepackets reach an amplitude of $|u|_{max} = 0.57\,\%$ when they are at $X \approx 850$ (see figures 3c and 4c). The distance from that location to spot formation (at $X \approx 1350$) is approximately $\Delta X \approx 500$ or $\Delta x \approx 115$ cm. This is comparable to $\Delta x \approx 100$ cm in the L case of Cohen *et al.* (1991) which registered an amplitude of 0.6 % at its first measurement station at $x = 170$ cm and suffered a major loss of coherence marking the onset of the turbulence at $x = 270$ cm.

Figure 5(a) shows the profile view of the u-initiated turbulent spot at $T = 2674$ and the instantaneous local wall skin friction coefficient along its centreline. The profile view shows that the turbulent spot overhangs the wall at its leading edge, which is consistent with experimental observations. The fluctuations overshoot the boundary layer in an irregular and intermittent manner and the approximate mean side profile of the spot is consistent with published data (Wygnanski, Sokolov & Friedman 1976). The instantaneous local wall skin friction coefficient in figure 5(b) reflects the nature of intermittency and localization within the turbulent spot, comprising burst regions

of high skin friction and fluctuations at different scales. The ensemble-averaged skin friction coefficients for laminar and fully developed turbulent boundary layers (both assumed to start from plate's leading edge at $X = 0$) are plotted for comparison in figure 5(b). These are calculated in accordance with the established formulae:

$$C_f^l = 0.664(Re_x)^{-1/2} \quad \text{(laminar)}, \tag{3.1a}$$

$$C_f^t = 0.455(\ln(0.06Re_x))^{-2} \quad \text{(fully developed turbulence)}, \tag{3.1b}$$

where $Re_x = U_\infty x/v$ (see White 1991). The computed local skin friction coefficient curve adheres very closely to the laminar flow curve outside the domain of the wavepacket. Within the turbulent spot, the local skin friction coefficient spikes up very sharply above the laminar values to values characteristic of a fully turbulent boundary layer. The average wall skin friction value under the spot is somewhat lower than the mean value for a fully developed turbulent boundary layer. This is not surprising, however, because here we are having only a single newly-formed turbulent spot in an otherwise laminar boundary layer, whereas a fully developed turbulent boundary layer is derived from the saturation of mature turbulent spots.

3.2. *Spectral analyses*

Flow quantities were analysed by double Fourier transforms (DFTs) in time and space. The analyses involve fast Fourier transform (FFT) in the time domain and DFT in the space domain. The bandwidth of the signals before sampling was limited to less than half of the sampling rate in accordance with the Nyquist criterion. The frequency–spanwise wavenumber (ω, β) spectra of the disturbance velocity components at different x-locations along the boundary layer are given in figures 6–7 and 10–11 for the u- and v-initiated wavepackets, respectively. Figures 8 and 12 show the (α, β) wavenumber spectra of the wavepackets at various time instants/stages in its evolution – they are derived from the analysis of a rectangular region at $y/\delta \approx 0.62$ containing the complete wavepacket, when its centre coincides approximately with the designated X-stations. These spectral plots are presented in terms of frequency and wavenumbers based on the global length scale δ_0, which is the displacement thickness at the initiation source. The spectral properties of the dominant two-dimensional and three-dimensional wave modes in the u- and v-initiated wavepackets are summarized in table 1. The tabulated data are derived primarily from the u-velocity spectra (which contain the larger part of the wave energy) and presented in terms of the local displacement thickness length scale $\delta(x)$. Since individual wave in Fourier integral essentially contains zero energy, the term 'mode(s)' is used here to connote a narrow band of waves in the spectral vicinity of the mode(s). The results in columns 2–4 of table 1 are representative of waves in the linear to very early subharmonic growth stages, while columns 5–7 are applicable to the primary subharmonic phase. Columns 8 and 9 present properties of the waves in the late-to-post subharmonic stages, where the leading two-dimensional modes are becoming non-distinct.

3.2.1. *Quasi-linear growth*

The growth of the wavepackets up to $X \approx 800$ is predominantly linear. A detailed comparison with the predictions of linear stability theory (LST), carried out in § 3.3, shows that some low-frequency oblique waves are undergoing weakly nonlinear growth as early as $X \approx 600$ while the bulk of other waves are developing linearly. More precisely, the growth of the wavepacket may be described as 'quasi-linear'.

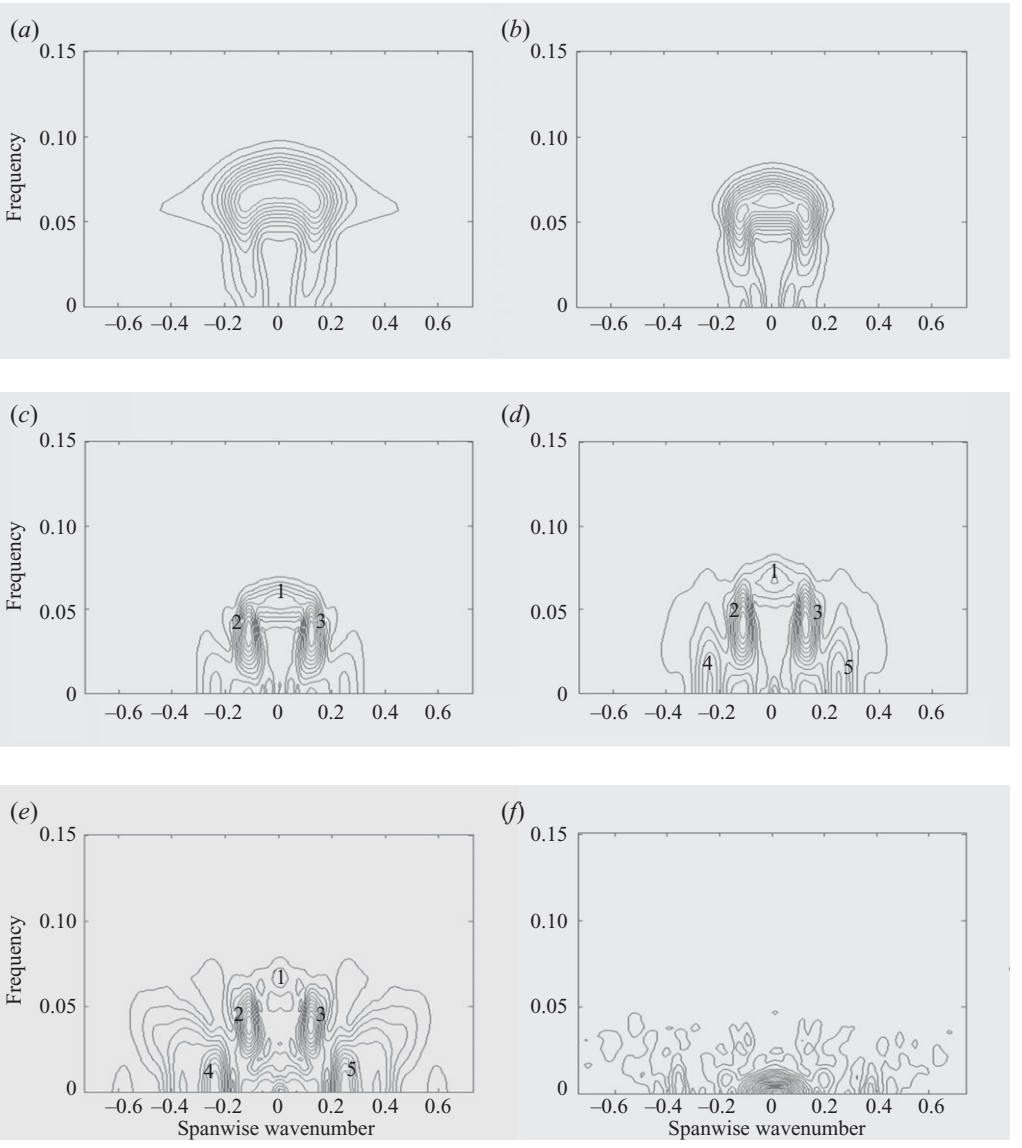

FIGURE 6. Spanwise wavenumber β versus frequency ω spectra of u at $y/\delta \approx 0.62$ (u-initiated wavepacket) at different locations: (*a*) $X = 690$; (*b*) $X = 863$; (*c*) $X = 1122$; (*d*) $X = 1208$; (*e*) $X = 1294$; (*f*) $X = 1380$. Here δ denotes the local displacement thickness.

Henceforth, we shall use the term quasi-linear to qualify this stage of wavepacket development. Figures 6(*a*,*b*) and 7(*a*,*b*) show the frequency–spanwise wavenumber (ω, β) spectra of the u- and v-velocity components of the u-initiated wavepacket as it evolves from $X = 690$ towards the late linear (or early subharmonic) stage at $X = 863$. The dominant wave is two-dimensional with frequency ω^{2D}, based on the δ_0, varying from 0.070 to 0.064 over the range. When rescaled by the local displacement thickness $\delta(x)$, the non-dimensional local frequency ω_δ^{2D} is remarkably constant at 0.1. The dominant two-dimensional frequency of $\omega_\delta^{2D} = 0.1$ was also recorded for the dominant two-dimensional disturbance modes in the experiments of Medeiros &

X	560	690	863	949	1035	1122	1208	1260
R_δ	1311	1454	1625	1705	1781	1854	1924	1965
u-initiated wavepacket, $y/\delta(x) \approx 0.62$								
ω_1^{2D}		0.098	0.100	0.100	0.099	0.099	0.129	–
α_1^{2D}		0.285	0.291	0.297	0.303	0.303	0.289	0.267
$\omega_{2,3}^{3D}$		–	0.088	0.082	0.075	0.065	0.074	0.077
$\alpha_{2,3}^{3D}$		–	0.262	0.244	0.213	0.185	0.160	0.148
$\beta_{2,3}^{3D}$		–	0.182	0.194	0.208	0.218	0.225	0.228
v-initiated wavepacket, $y/\delta(x) \approx 0.62$								
ω_1^{2D}		0.096	0.102	0.100	0.097	0.097	0.099	–
α_1^{2D}		0.267	0.274	0.268	0.273	0.278	0.278	0.275
$\omega_{2,3}^{3D}$		0.085	0.089	0.084	0.076	0.058	0.059	0.0607
$\alpha_{2,3}^{3D}$		0.236	0.245	0.218	0.189	0.167	0.157	0.159
$\beta_{2,3}^{3D}$		0.193	0.196	0.205	0.208	0.205	0.214	0.232
v-initiated wavepacket, $y/\delta(x) \approx 1.2$								
ω_1^{2D}	0.093	0.096	0.099	0.100	0.102	0.100	0.102	
α_1^{2D}	0.246	0.265	0.277	0.277	0.279	0.267	0.272	
$\omega_{2,3}^{3D}$	0.080	0.086	0.082	0.082	0.069	0.065	0.061	
$\alpha_{2,3}^{3D}$	0.199	0.230	0.231	0.219	0.206	0.161	0.154	
$\beta_{2,3}^{3D}$	0.206	0.179	0.199	0.209	0.218	0.197	0.202	

TABLE 1. Spectral data of u-velocity fluctuations for the dominant two-dimensional and three-dimensional modes. Data presented are based on the local displacement length scale $\delta(x)$.

Gaster (1999*b*). A corresponding $\omega_\delta^{2D} \approx 0.09-0.10$ can also be discerned in the results of Cohen *et al.* (1991) for their most energetic two-dimensional waves.

Figures 6(*a*) and 7(*a*) show that the oblique waves are spectrally contiguous with the dominant two-dimensional mode. Broadband oblique wave modes are also evident in the spectral plots of the cited experiments. The very weak low-frequency components of oblique waves (not part of unstable linear spectrum) may be caused by parametric amplification of background noises/waves according to Kachanov & Levchenko (1984). As the u-initiated wavepacket evolves into the late linear or early subharmonic stage (figures 6*b* and 7*b*), both the dominant two-dimensional mode and its contiguous spectrum of oblique wave modes are amplified in unison. In particular, the oblique wave spectra begin to extend towards lower frequency. This is also true for the spectra of the v-initiated wavepacket in figure 10(*a*,*b*). Indeed the u-velocity spectra of both wavepackets also reveal the presence of some very low-frequency components. They are not replicated in the v-velocity spectra, however, because the low-frequency v-velocity fluctuations have very low energy at this early stage.

3.2.2. *Subharmonic wave growth*

The dominant two-dimensional frequency of $\omega_\delta^{2D} \approx 0.1$ (from the linear stage) was maintained well into the subharmonic stage in the experiments of Cohen *et al.* (1991). The same could also be said for the numerous experiments conducted by Medeiros & Gaster (1999*b*) in their study on subharmonic wave production in evolving wavepackets. The results of the present simulations in figure 15(*a*) for both the u- and v-initiated wavepackets also reflect this preferred frequency $\omega_\delta^{2D} \approx 0.1$ for

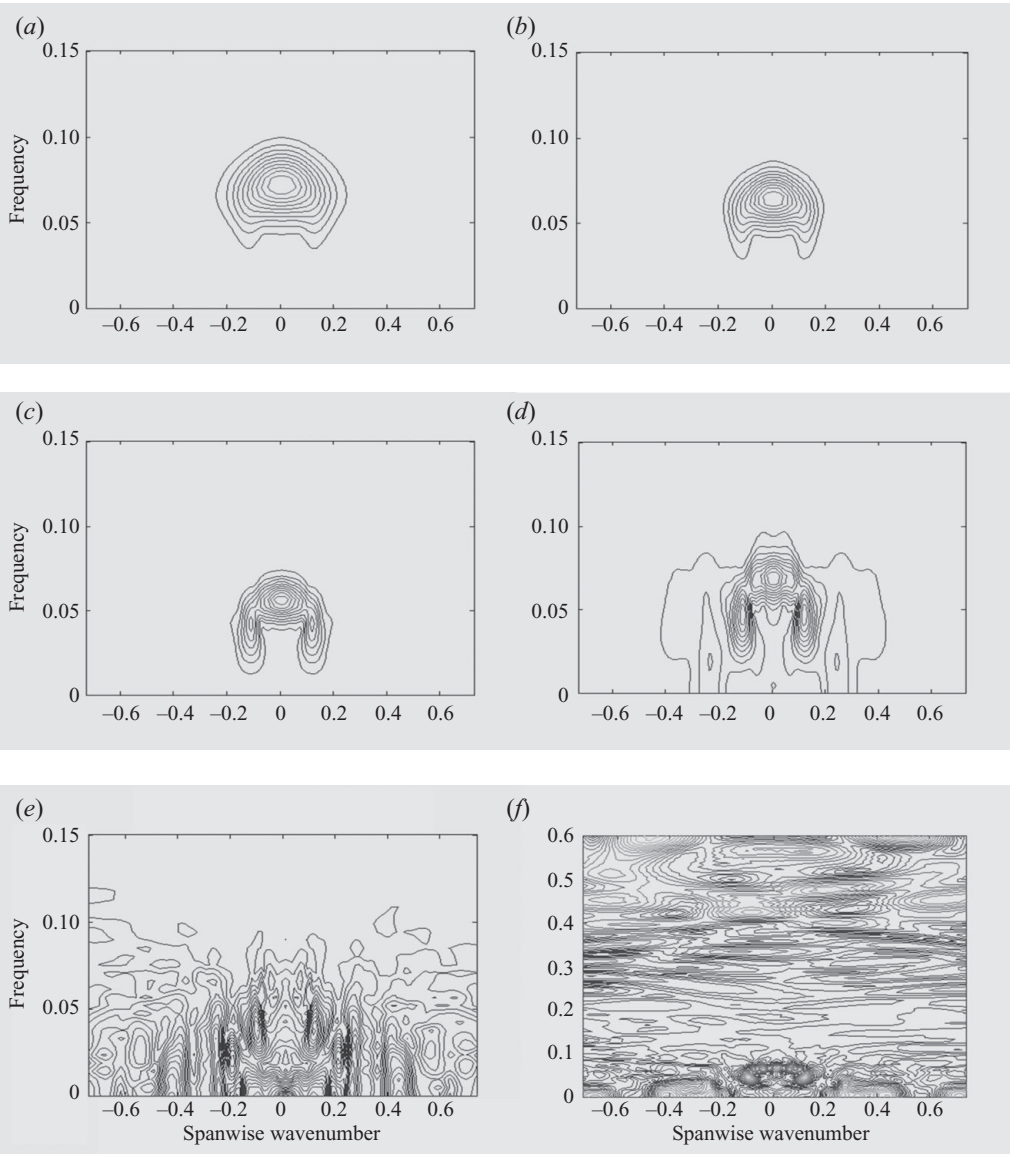

FIGURE 7. Spanwise wavenumber β versus frequency ω spectra of wall-normal disturbance velocity v at $y/\delta \approx 0.62$ (u-initiated wavepacket) at different locations: (a) $X = 690$; (b) $X = 863$; (c) $X = 1122$; (d) $X = 1208$; (e) $X = 1294$; (f) $X = 1380$.

the dominant two-dimensional mode over the bulk of the evolution history, except perhaps in the late subharmonic stage, where ω_δ^{2D} appears to rise sharply in the case of the u-initiated wavepacket.

The subharmonic phase is characterized by the emergence and growth of a dominant oblique wave pair whose frequency $\omega_{2,3}^{3D}$ is less than the dominant two-dimensional (fundamental) frequency ω_1^{2D}. Figures 6(a–c) and 10(a–c) show how a distinctive and dominant subharmonic oblique wave pair gradually emerges from the expanding three-dimensional spectra, contiguous to the dominant two-dimensional mode, for the two wavepackets. The dominant subharmonic oblique wave pair acquires

comparable amplitude with the fundamental two-dimensional wave by $X \approx 1035$. Table 1 and figure 15 summarize the characteristics of the triad of waves, comprising the fundamental two-dimensional wave and the oblique wave pair, as they evolve from the early subharmonic growth stage ($X \approx 860$) through to the late subharmonic stage ($X \approx 1208$). The component waves of the triad are marked by subscript 1 for the fundamental two-dimensional wave and subscripts 2 and 3 for the oblique wave pair, as shown in figure 6(*c*,*d*).

Three-wave subharmonic resonance between the fundamental two-dimensional wave and the three-dimensional oblique wave pair is governed by the following frequency and wavenumber conditions:

$$\omega_1^{2D} = 2\omega_{2,3}^{3D}, \quad \alpha_1^{2D} = 2\alpha_{2,3}^{3D} \quad \text{and} \quad \beta_1^{2D} = 0 = \beta_2^{3D} + \beta_3^{3D}. \tag{3.2a–c}$$

Figure 15(*b*,*c*) shows that the frequency and wavenumber ratios, $\omega_{2,3}^{3D}/\omega_1^{2D}$ and $\alpha_{2,3}^{3D}/\alpha_1^{2D}$, vary from about 0.9 to 0.6 as the *u*- and *v*-initiated wavepackets evolve downstream through the subharmonic instability stage from $X \approx 860$–1208 ($x = 200$–280 cm). They are not close to the value of 0.5 that one would expect from the fulfilment of the subharmonic resonant wave condition (3.2). Nonetheless, the wavepackets appear to be spontaneously evolving towards resonance, although exact resonance between the dominant two-dimensional wave and the three-dimensional wave pair in accordance with wave relations (3.2) is not quite achieved even as the waves enter the late subharmonic stage at $X = 1208$ ($x = 280$ cm). Frequency ratios $\omega_{2,3}^{3D}/\omega_1^{2D} \approx 0.55$ may be deduced from figures 4 and 8 of Cohen *et al.* (1991) for their S and L cases respectively in the late subharmonic stages.

Medeiros & Gaster (1999*b*) observed that the subharmonic frequency ratios $\omega_{2,3}^{3D}/\omega_1^{2D}$ were greater than the value of 0.5 in almost all the wavepackets that they had studied, which were initiated with different phase contents. These appear to tend towards the factor of 0.5 as the oblique wave pairs strengthened downstream, but never quite reaching the value (see their figure 4). The spectral peaks of their three-dimensional waves have spanwise wavenumber $\beta_\delta \approx 0.2$, which is in very good agreement with the same for the primary subharmonic stages ($X = 863$–1035) of simulated wavepackets given in table 1 at the same height of $y/\delta \approx 0.62$. The corresponding $\beta_\delta \approx 0.25$ for the S case of Cohen *et al.* (1991). In general, the present simulation results at $y/\delta \approx 0.62$ show a slowly increasing spanwise wavenumber β_δ for the dominant three-dimensional mode as the wavepackets evolve downstream. For the larger-amplitude L-case, Cohen *et al.* (1991) quoted streamwise wavenumbers of $\alpha_1^{2D} \approx 0.3$ and $\alpha_{2,3}^{3D} \approx 0.16$ for the dominant two-dimensional and three-dimensional waves respectively in its subharmonic stage at $x = 230$ cm – these were estimated by fitting LST solutions to experimental data. These compare quite well with the values of $\alpha_1^{2D} \approx 0.27$–$0.30$ and $\alpha_{2,3}^{3D} \approx 0.15$–$0.18$ given in columns 7 and 8 of table 1 for the corresponding subharmonic stage ($X = 1122$–1208, $x = 260$–280 cm); it is pertinent to note that the L-case wavepacket arrived at the same subharmonic stage at a smaller $x = 230$ cm owing to its larger initial amplitude.

The above results suggest that subharmonic wave production in wavepackets may not be simply explained on the basis of Craik resonance (3.2). The theory of Herbert (1988) provides for frequency and wavenumber detuning when resonance is not exact. A well-defined detuned pair of frequency peaks ($\omega_C \pm \Delta\omega$) had been observed for ribbon-excited waves in the experiments of Kachanov & Levchenko (1984). More recently, Sartorius *et al.* (2006) found that positively frequency-detuned periodically driven subharmonic modes might be more strongly amplified than those without

detuning. However, Medeiros & Gaster (1999*b*) had observed that there was no obvious evidence of conjugate frequency and/or wavenumber pairing in the spectra of the many wavepackets that they had studied, which could plausibly explain their role in subharmonic wave production. We have also found no corroborative evidence of frequency and/or wavenumber detuning in the results. It is possible that detuned instabilities might not work well in the complex and highly transient wave environment of a wavepacket, where a large continuum of two-dimensional/three-dimensional waves compete for dominance, as opposed to the more controlled environment of selective periodic excitations.

Figure 15(*d*) compares the downstream phase speeds of the dominant three-dimensional and two-dimensional modes in the *u*- and *v*-initiated wavepackets. The ratios $c_{2,3}^{3D}/c_1^{2D} \approx 1$ over the whole subharmonic stage (largest deviations from 1 occur at station $X = 1035$ in all three sets of results). This would not be surprising if the wave triads had satisfied the subharmonic resonant wave condition (3.2), since that would ensure that the condition $c_{2,3}^{3D}/c_1^{2D} = 1.0$ is automatically fulfilled. However, the converse need not be true. The condition $c_{2,3}^{3D}/c_1^{2D} \approx 1.0$ is fairly well satisfied throughout the subharmonic stage even though the frequency and wavenumber ratios, $\omega_{2,3}^{3D}/\omega_1^{2D}$ and $\alpha_{2,3}^{3D}/\alpha_1^{2D}$ (figure 15*b*,*c*), are substantially higher than the resonance value of 0.5. This suggests that a sustained critical-layer-driven mechanism, a weaker condition than triad resonance given by (3.2), may be the source of subharmonic wave production in the boundary layer.

3.2.3. *Post-subharmonic and breakdown phase*

The dominant subharmonic modes in the *u*- and *v*-initiated wavepacket surpass the fundamental two-dimensional wave in amplitude by $X \approx 1035$. The next stage of evolution is marked by the generation of low-frequency *u*-velocity fluctuations through nonlinear interaction, which is evident in figures 6(*c*,*d*) and 8(*b*). Thus, one may note that the interaction of the dominant oblique waves 2 and 3 gives rise to the difference modes 4 and 5, $(0, \pm 2\beta_2^{3D}, 0) = \pm(\alpha_2^{3D}, \beta_2^{3D}, \omega_2^{3D}) \mp (\alpha_2^{3D}, \beta_3^{3D}, \omega_3^{3D})$, which have near-zero frequency and spanwise wavenumbers ($\pm 2\beta_2^{3D}$) that are twice those of the dominant subharmonic modes 2 and 3. This process is further enhanced by the increasing strength of the dominant subharmonic modes. The wavepacket is now entering the post-subharmonic stage, whereby the interaction between the difference modes $(0, \pm 2\beta_2^{3D}, 0)$ results in near-zero and zero wavenumber and frequency mode (0,0,0) that may be discerned in figures 6(*e*), 7(*e*) and 8(*c*). This stage is distinguished by the sideway proliferation of higher harmonics along the β axis in figures 6(*d*,*e*), 7(*d*, *e*) and 8(*b*, *c*), and most clearly captured in figure 8(*c*). This is essentially an oblique-wave (β-)cascade as there is no concomitant expansion in the higher harmonics of the streamwise wavenumber α and frequency ω. The β-cascade was observed in the experiments of Breuer *et al.* (1997). What follows becomes increasingly difficult to decipher in detail – at this stage, it is no longer possible to discern a distinct dominant two-dimensional mode.

The strengthening of the near-zero frequency modes within the wavepacket leads to increasing three-dimensional local distortion of the base flow (see figure 2.16 in Holmes *et al.* 1996, and Lundbladh *et al.* 1994). It is associated with the rapid growth of the Λ-vortex (a structure of some temporal permanence) at this stage. The Λ-vortex convects with the wavepacket, so that to an external observer the distortion would appear as a spatially amplifying localized three-dimensional modulation of the base flow field. The further development of the Λ-vortex into a loop (or hairpin-like) vortex (Perry, Lim & Teh 1981) due to stretching by the base flow and vortex

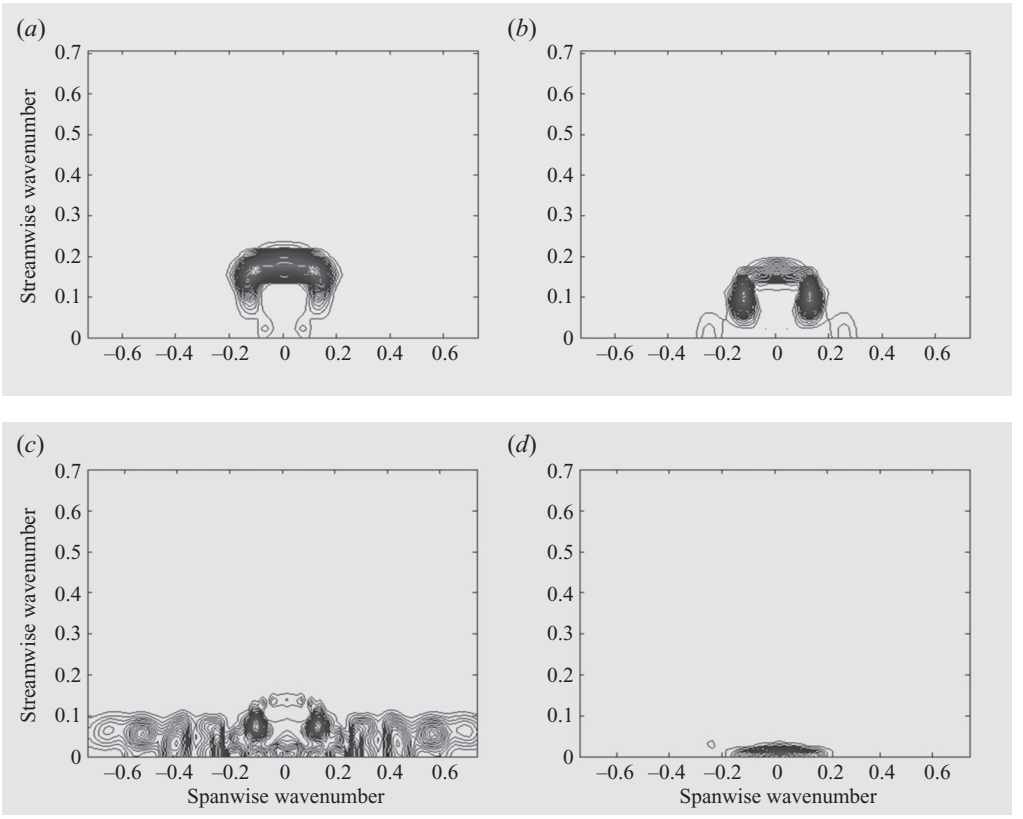

FIGURE 8. Streamwise wavenumber α versus spanwise wavenumber β spectra of u at $y/\delta \approx 0.62$ for the u-initiated wavepacket at times: (*a*) $T = 1300$ ($X = 850$); (*b*) $T = 2046$ ($X = 1125$); (*c*) $T = 2417$ ($X = 1260$); (*d*) $T = 2674$ ($X = 1410$). X denotes the approximate streamwise position of the centre of the wavepacket.

self-induction, and the formation of ring-like vortices possibly due to a Crow-type instability (Crow 1970; Moin, Leonard & Kim 1986; Rist, Muller & Wagner 1998; Borodulin, Kachanov & Roschektayev 2006), lead eventually to the breaking down of hitherto regular wavepacket structures.

The wavepacket breakdown that follows is marked by further strengthening of the low-frequency modes and ultimately by the rapid proliferation of higher ω and α modes generated by evolving sums and differences of extant wave modes. The v-velocity spectrum at $X = 1380$ ($x = 320$ cm) in figure 7(*f*) shows a strong presence of high-frequency waves, clearly indicating that the breakdown of the wavepacket had already begun. Figure 9(*c*) gives the corresponding frequency power spectrum. The spectral expansion to higher frequency is not so obvious in the u-velocity spectrum in figure 6(*g*) (compared to figure 7*f*). This is because a large part of the u-disturbance wave energy is concentrated in the low-frequency components at this stage, as may be seen in figure 9(*b*,*c*). Figure 9(*c*), on the other hand, shows a more even spread of v-disturbance wave energy across the frequency spectrum of the incipient spot. The flattish spread of the (α, β) spectrum in figure 8(*d*) indicates that the energetic u-disturbances in the incipient turbulent spot are longish/streaky in the stream direction. This is in accord with the u-velocity visualization of the incipient turbulent spot in

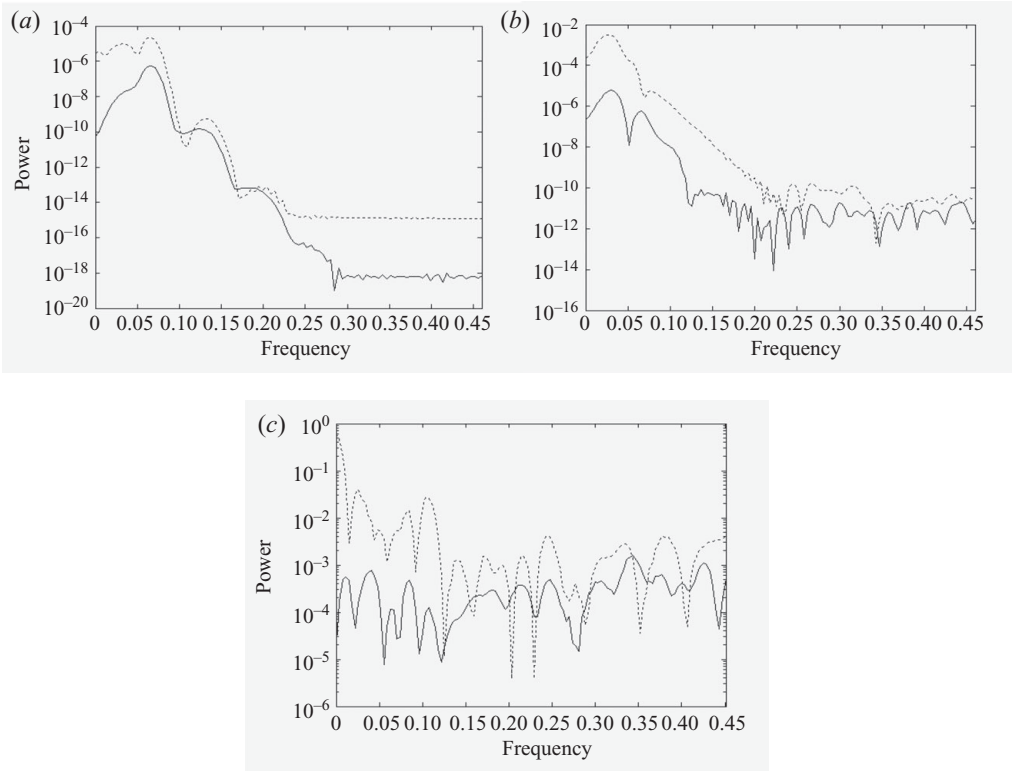

FIGURE 9. Power spectra of u and v as a function of frequency ω along the centreline at $y/\delta \approx 0.62$ at downstream locations: (a) $X = 863$; (b) $X = 1208$; (c) $X = 1380$. Disturbance velocity: streamwise u, ·····; wall-normal v, ——— (u-initiated wavepacket).

figure 3(i,j) at $y/\delta = 0.62$ and at other heights. In contrast, the v- and w-velocity disturbances of the incipient spot comprise largely fine-scale structures at all heights.

Except for differences of details, selected spectra of the v-initiated wavepacket in figures 10–12 reveal closely similar spectral evolution as the u-initiated wavepacket. Figures 10(d,e) and 12(c) show clearly the development of near-zero frequency longitudinal ($\alpha \approx 0$) u-velocity fluctuations at twice the spanwise wavenumber of the dominant oblique wave pair. The expansion of the β-spectrum follows (figure 11c,d) closely on the heels of this process. For both the u- and v-initiated wavepackets, significant loss of structural regularity (and presence of high-frequency fluctuations) is clearly evident by $X \approx 1380$ or $x \approx 320$ cm (see figures 3i, 7f and 11d). The corresponding breakdown stage in the S-case experiment of Cohen *et al.* (1991) occurred further downstream at $x \approx 350$ cm due to its slightly lower initial amplitude.

3.3. *Comparison with linear stability theory*

In this section we examine the development of the wavepacket in the context of LST. Figure 13 compares the spatial growth of selected two-dimensional and three-dimensional wave modes in the simulated v-initiated wavepacket against the predictions of LST. The point data represent the spectral amplitudes of waves of fixed frequency ω and spanwise wavenumber β (based on the global length scale δ_0) obtained from the spectral analyses of u-velocity signals across the domain (spanwise)

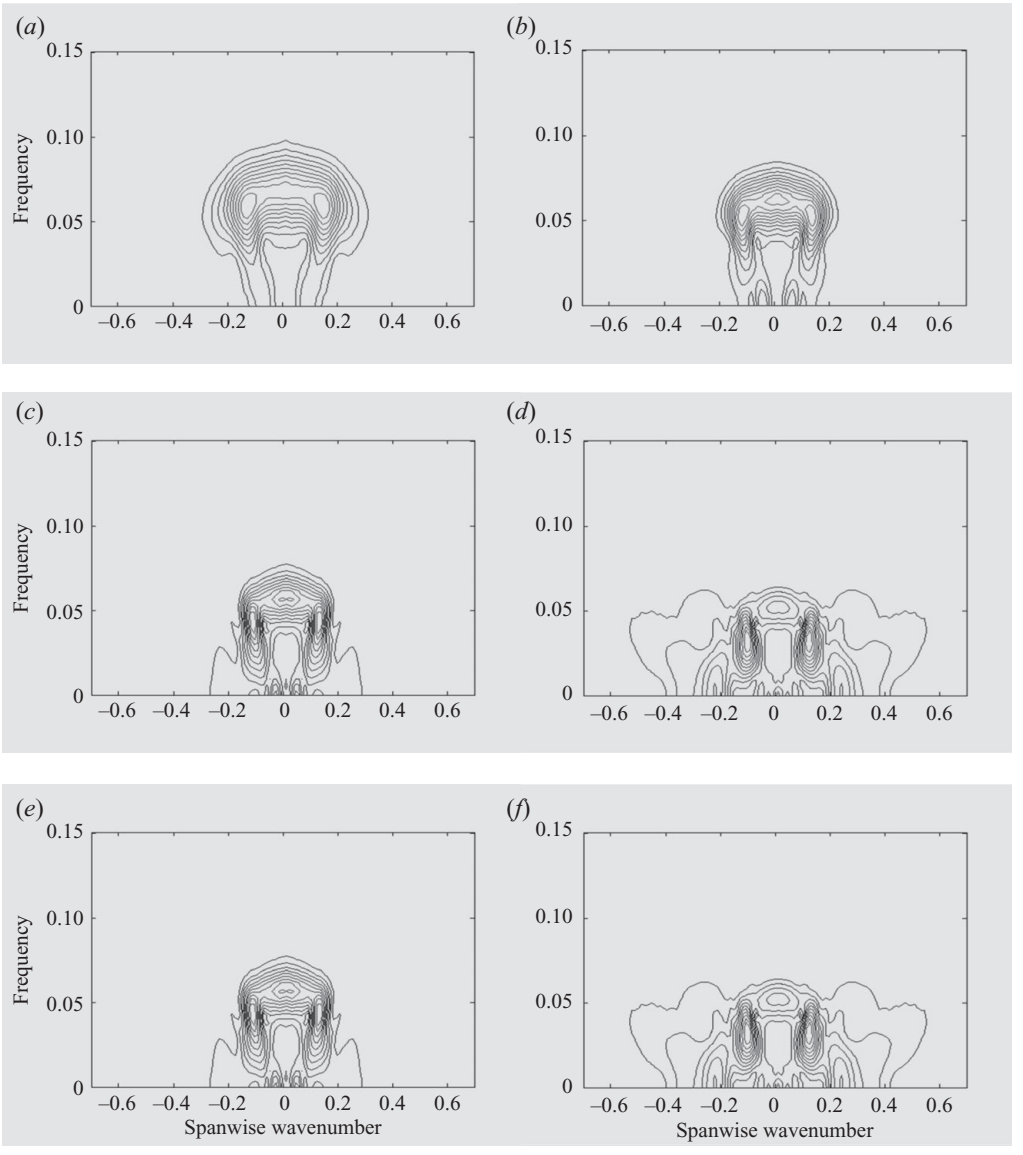

FIGURE 10. Spanwise wavenumber β versus frequency ω spectra of u at $y/\delta \approx 0.62$ (v-initiated wavepacket) at different locations: (*a*) $X = 690$; (*b*) $X = 863$; (*c*) $X = 1035$; (*d*) $X = 1208$; (*e*) $X = 1294$; (*f*) $X = 1380$. Here δ is the local displacement thickness of the boundary layer.

at the height $y/\delta \approx 0.62$. The corresponding curves are spatial growth curves derived from LST, duly shifted for an optimal match with the wavepacket data. Results of four spanwise wavenumbers $\beta = 0.0$, 0.05, 0.125 and 0.22 and four frequencies $\omega = 0.04$, 0.05, 0.06 and 0.07 are presented.

Figure 13(*a*) shows that there is good agreement between the spectral wave amplitudes and LS predictions for two-dimensional wave modes at all the frequencies from linear to the early subharmonic stages from $X = 450$ to 863 ($Re_\delta = 1172$–1626). Indeed, the agreement extends well into the principal subharmonic growth stage

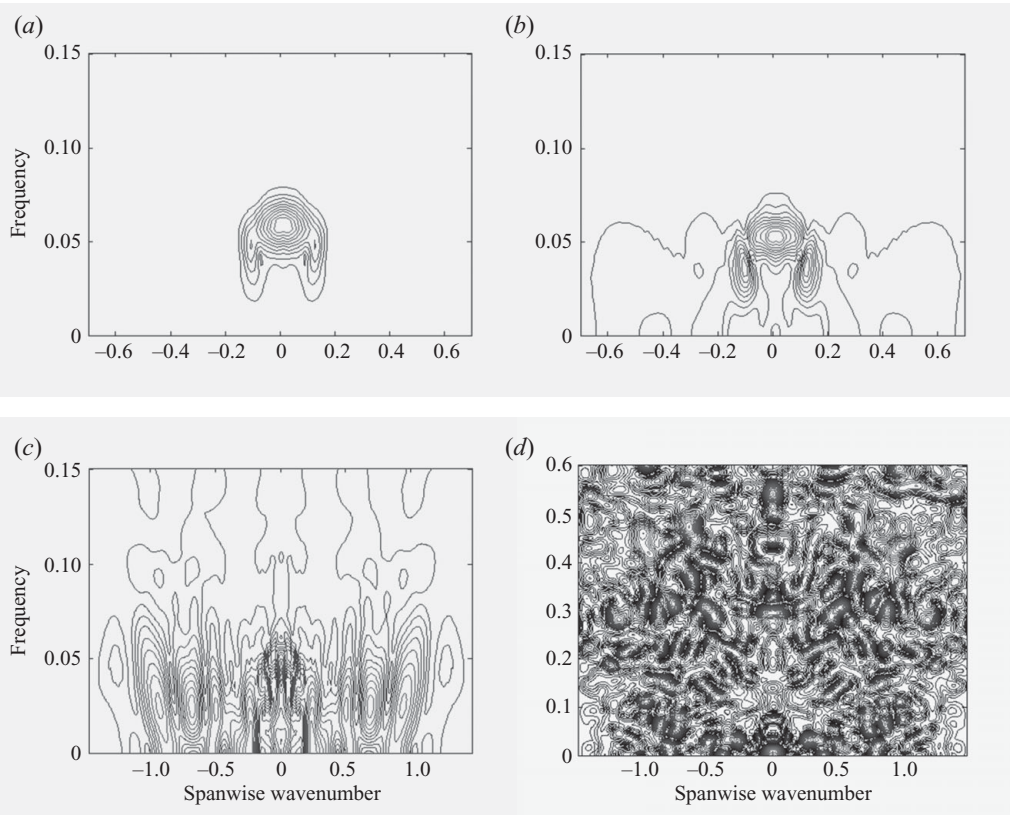

FIGURE 11. Spanwise wavenumber β versus frequency ω spectra of wall-normal velocity v at $y/\delta \approx 0.62$ (v-initiated wavepacket) at different locations: (*a*) $X = 1035$; (*b*) $X = 1208$; (*c*) $X = 1294$; (*d*) $X = 1380$.

($X \approx 950$–1208) for all except the frequency of $\omega = 0.07$, where more apparent deviation may be observed for $X > 863$.

Figure 13(*a*) also compares the growth of the most amplified or dominant two-dimensional waves in the wavepacket (marked by black circular dots) against the LS prediction for a mode with a fixed non-dimensional local frequency of $\omega_\delta^{2D} = 0.099$, applied from $X = 640$–1208 ($Re_\delta \approx 1400$–1900). The frequency $\omega_\delta^{2D} \approx 0.099$ incidentally corresponds to the average frequency of two-dimensional modes along the 'maximum linear amplification envelope' given in figure 4 of Jordinson (1970) ($\omega_\delta^{2D} \approx 0.102$–$0.096$ for the Re_δ range). The good agreement shows that, after a short initial phase of fairly rapid growth away from the source, the dominant two-dimensional waves in the wavepacket evolve more or less along the growth trajectory of the maximum linear amplification envelope. The initial growth phase (up to $X \approx 640$) may be influenced by the spectral composition of the wavepacket at initiation. This tendency towards maximum linear amplification appears to be generic. It may thus explain why the dominant two-dimensional waves in the simulated wavepackets (in §§ 3.2.1–3.2.2) maintained a nearly constant local frequency of $\omega_\delta^{2D} \approx 0.1$ over the bulk of their evolution histories, as well as the persistent observations of the same frequency in the wavepacket experiments of Medeiros & Gaster (1999*b*) and Cohen *et al.* (1991). Cohen (1994) had earlier found that LST accurately predicted the growth of the most amplified two-dimensional waves in his experimental wavepackets. However, the

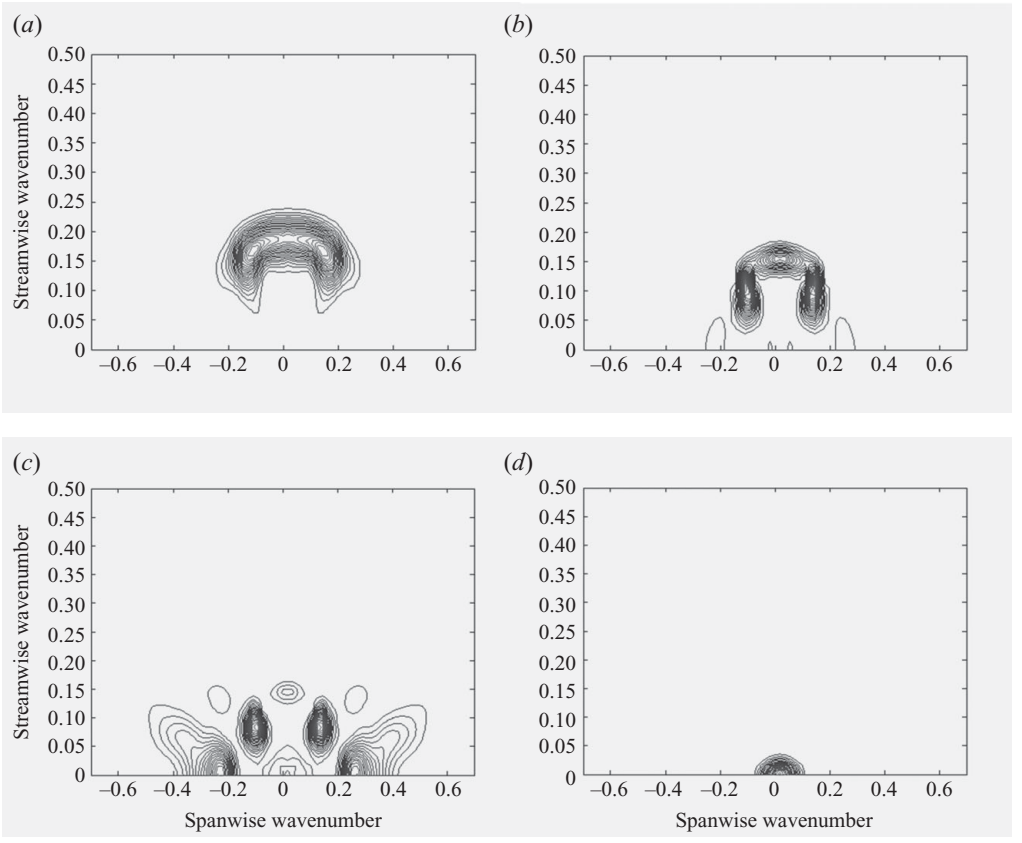

FIGURE 12. Streamwise wavenumber α versus spanwise wavenumber β spectra of u at $y/\delta \approx 0.62$ for the v-initiated wavepacket at times: (*a*) $T = 930$ ($X = 690$); (*b*) $T = 2046$ ($X = 1125$); (*c*) $T = 2417$ ($X = 1260$); (*d*) $T = 2788$ ($X = 1420$). Here X denotes the approximate streamwise position of the centre of the wavepacket.

specific frequency of $\omega_\delta^{2D} \approx 0.1$ and its approximate constancy over the experimental range were not discussed by him. Cohen's LS results also took into account the slow divergence of the boundary layer, whereas the present LS results were based on the locally parallel flow approximation.

Figure 13(*b–d*) shows the spatial growth of three-dimensional waves at fixed spanwise wavenumber β. In general, spatial growth of mildly oblique waves ($\beta = 0.05$, figure 13*b*) follows quite closely the predictions of the LST well into the subharmonic stage. The most amplified oblique waves have $\beta \approx 0.125$ (figure 13*c*). The mode with $\beta = 0.125$ and $\omega = 0.04$ amplifies by a factor of nearly 10^2 between $X = 450$ and 1208 ($Re_\delta = 1174$–1924), and is in fact spectrally close to the most amplified oblique wave mode at $X = 1208$ in the late subharmonic stage (see figure 10*d*). Waves in the lower-frequency band around $\omega \approx 0.04$ ($\beta = 0.125$) exhibit signs of deviating from the linear growth curves as early as $X \approx 600$ (well upstream of its upper neutral points). Hence, the development of the wavepacket is not fully linear even at this early growth stage. The evolution of these waves into the most amplified three-dimensional wave modes in the subharmonic stage may be seen to be a progressive rather than an abrupt event.

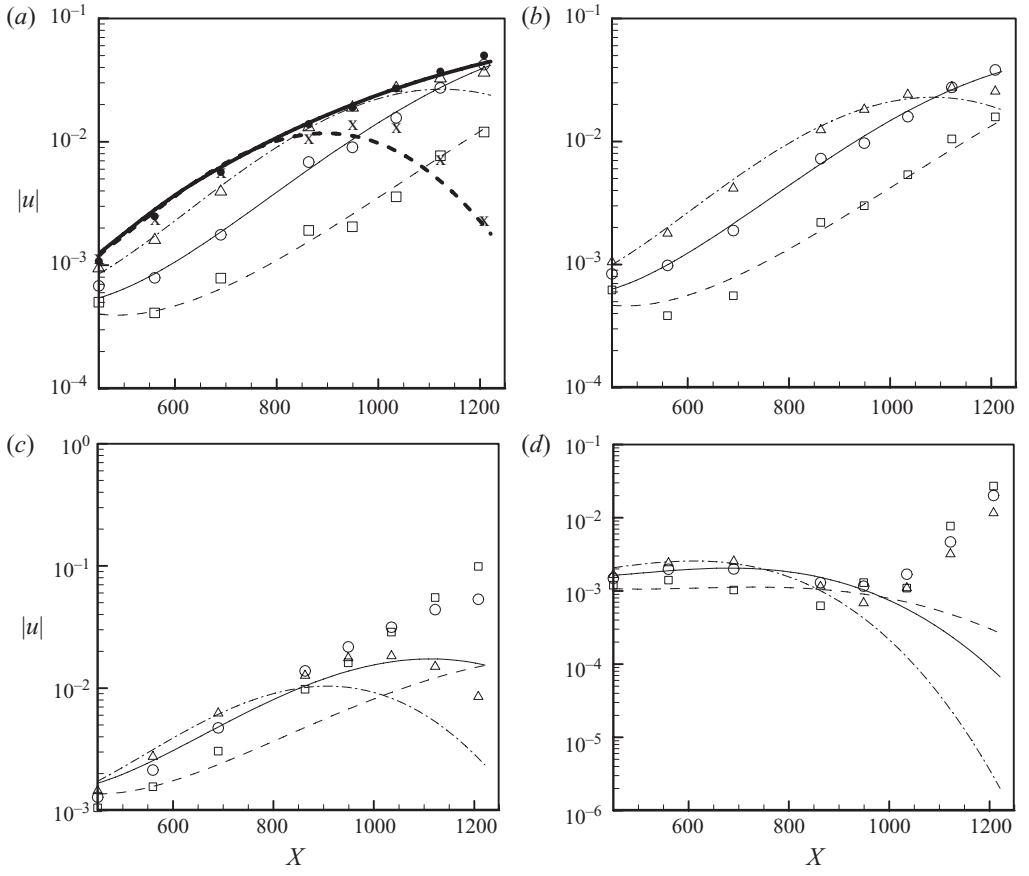

FIGURE 13. Comparison between the computed (symbols) and theoretical (lines) downstream growth of waves at various frequencies ω and spanwise wavenumbers β: (*a*) $\beta = 0$; (*b*) $\beta = 0.050$; (*c*) $\beta = 0.125$; (*d*) $\beta = 0.220$. Symbol/line: □/– – – ($\omega = 0.04$); ○/—— ($\omega = 0.05$); Δ/· - · - · ($\omega = 0.06$); × /▬ ▬ ($\omega = 0.07$); ●/▬▬ ($\omega_\delta = 0.100/0.099$). Theoretical results are based on linear theory. Here ω_δ is the frequency based on local displacement thickness δ.

Figure 13(*d*) shows that the growth of the highly oblique waves ($\beta = 0.22$) in the wavepacket is in accordance with LST up to about $X \approx 863$ ($Re_\delta \approx 1626$). By this time, they are already downstream of their branch II neutral points. Their growth accelerates considerably, however, during the ensuing subharmonic stage, reaching factors in the low 10s by the end of the stage. The most amplified oblique wave here ($\beta = 0.125, \omega = 0.04$), on the other hand, lingers close to the branch II neutral surface, on the upstream (linearly unstable) side, during the subharmonic stage. The above accords well with Cohen's (1994) findings that a group of highly amplified three-dimensional wave modes exhibit weakly nonlinear growth very early on in the linear growth stage, when most other waves are growing linearly. The rapid growth of highly oblique modes downstream of their branch II neutral points (as in figure 13*d*) has also been highlighted by Cohen (1994).

Velocity fluctuations of selected wave modes in the evolving wavepacket are presented in figure 14. Corresponding LS eigenfunctions are also presented for comparison (a single scaling factor was used for all the three velocity components of an LS eigenfunction). In general, there is remarkably sharp agreement between the

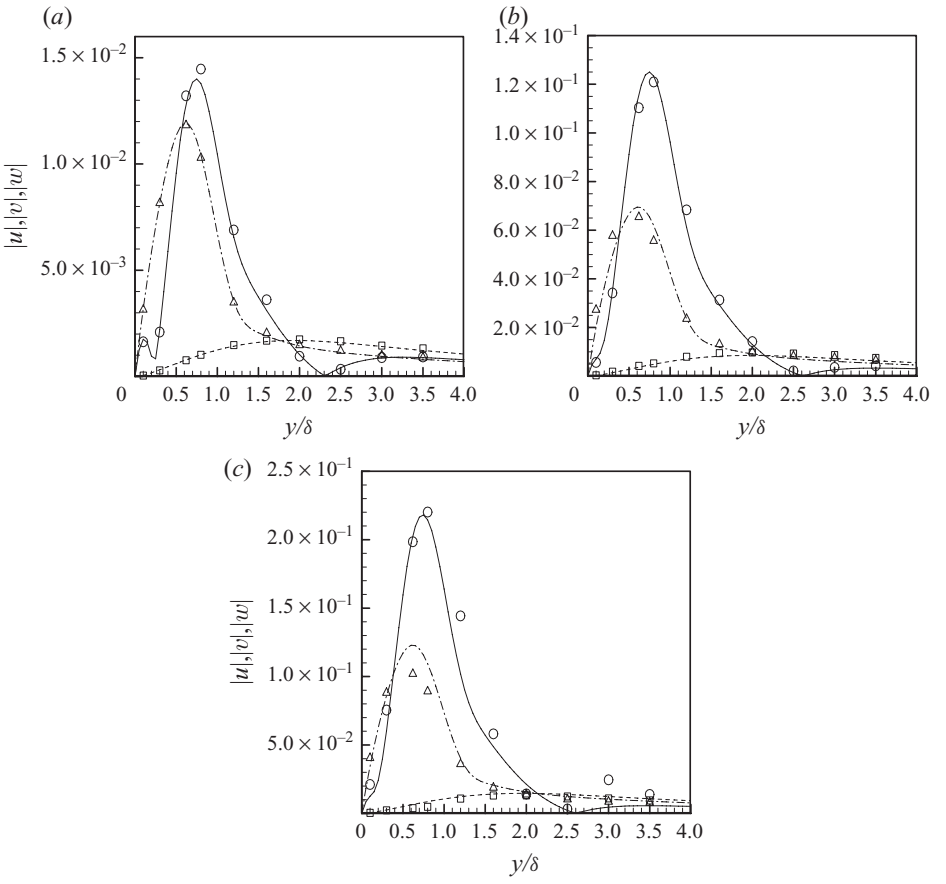

FIGURE 14. Comparison between the computed (symbols) and theoretical (lines) amplitude distributions of u, v and w for (a) $X = 863$, $\omega = 0.05$, $\beta = 0.125$; (b) $X = 1208$, $\omega = 0.03$, $\beta = 0.125$; (c) $X = 1294$, $\omega = 0.03$, $\beta = 0.125$. Symbol/line: ○/—— (u); □/- - - (v); Δ/-·-·-·- (w). Theoretical results are based on LST.

velocity fluctuations extracted spectrally from the wavepacket and corresponding LS eigenfunctions in the quasi-linear and early subharmonic stages. Figure 14(a,b) shows that the agreement between modal wavepacket fluctuations and LS eigenfunctions is very good even for the most highly amplified oblique wave modes at $\beta = 0.125$ over the whole of the subharmonic stage from $X \approx 863$–1208. The differences between the two, however, become more obvious as the wavepacket enters the post-subharmonic stage at $X = 1294$ (figure 14c). The close agreement between the wavepacket and LS eigenfunctions for the most amplified oblique modes had been noted by Cohen (1994).

3.4. *Subharmonic wave generation*

Corke & Mangano (1989) was probably the first to observe experimentally that three-dimensional plane disturbances could grow nonlinearly to significant amplitudes in a Blasius boundary layer despite not satisfying the subharmonic resonant-triad condition (3.2). Similar observations were subsequently made by Corke, Krull & Ghassemi (1992) and Williamson & Prasad (1993a, b) for wake flows. Wu & Stewart (1996) proposed a phase-locked interaction theory to explain this growth phenomenon and applied it to nonlinear interactions between two-dimensional and oblique

Rayleigh waves. While weaker than a resonant-triad, the phase-lock mechanism could nevertheless promote the rapid growth of oblique wave modes that have the same wave speed $c^{3D} = c^{2D}$ as the fundamental two-dimensional mode. This is essentially a critical-layer-based mechanism. More recently, Wu, Stewart & Cowley (2007) extended the phase-locked theory to Tollmien–Schlichting waves in a Blasius boundary layer. According to this theory, the interaction between a two-dimensional planar mode and a pair of oblique waves could result in the super-exponential growth/decay of the oblique waves if there is a small but non-zero mismatch in their wave speeds $c^{3D} \approx c^{2D}$. Moreover, for any given two-dimensional planar mode $(\alpha^{2D}, 0)$ and oblique wave pair $(\alpha, \pm\beta)$ that satisfy the Squire's wavenumber condition

$$\tilde{\alpha} = \sqrt{\alpha^2 + \beta^2} = \alpha^{2D} \quad \text{(to the leading order)}, \tag{3.3}$$

there is an 'optimal' phase speed mismatch which gives the maximum rate of super-exponential growth. The relaxed matching conditions allow the new phase-locked mechanism to operate under much less restrictive conditions than that required for triad resonance (3.2). Significantly, the new phase-locked theory shows that a single two-dimensional mode can act as a catalyst for the super-exponential growth of a broad spectrum of three-dimensional waves that share 'approximately' the same phase speed. Recent experiments by Borodulin, Kachanov & Koptsev (2002*a*, *c*) in which a single two-dimensional primary wave was found to amplify a broad spectrum of three-dimensional background disturbance waves having about the same phase speeds seem to support the theory. The new phase-lock theory of Wu *et al.* (2007) thus offers a mechanism that may explain the broadband nature of nonlinear wave growth and selection in a boundary layer. Nonetheless, the catalytic role of the fundamental two-dimensional wave in transferring energy from the mean flow to the three-dimensional waves is not an entirely new idea, and had been discussed by Orszag & Patera (1983) in their numerical study of wall-bounded shear flows. It is also pertinent to note that Herbert's (1983, 1988) theory of parametric resonance presumed an 'equilibrium' two-dimensional fundamental wave. Broadband amplification of three-dimensional waves by the two-dimensional fundamental wave had also been noted in the experiments of Kachanov & Levchenko (1984).

Although the analysis of Wu *et al.* (2007) had been carried out for plane waves, the theory is clearly relevant to the wavepackets here. The spectral results of the preceding section (see figure 15*d*) show that the x-phase speeds of the dominant two-dimensional and three-dimensional modes of the wavepackets track each other fairly closely ($c^{3D}/c^{2D} \approx 1.0$) over much of the nonlinear growth stages, in fact, until a distinctive dominant two-dimensional mode could no longer be clearly discerned from the spectral data. Figure 15(*e*) further shows that the approximate match in phase speeds is also corroborated by corresponding fulfilment of the Squire wavenumber condition (3.3) to a high degree over the nonlinear growth stage from $X \approx 949$–1260 for both the u- and v-initiated wavepackets. The agreement (or degree of mismatch) is largely within 10 % for phase speeds and 5 % for Squire wavenumber condition (3.3) for the u-initiated wavepacket and 10 % for the v-initiated wavepacket. Measurement errors associated with the identification of spectral peaks are typically quite small at around 1–2 %. Phase-speed differences of up to 10 % may also be observed in the experimental results of Borodulin *et al.* (2002*c*), as reproduced in Wu *et al.* (2007). Figure 15(*f*) shows that the propagation angles θ of the dominant three-dimensional modes evolve progressively towards 60° as the u- and v-initiated wavepackets develop through the subharmonic stage, reaching values of about 56° and 57° in the

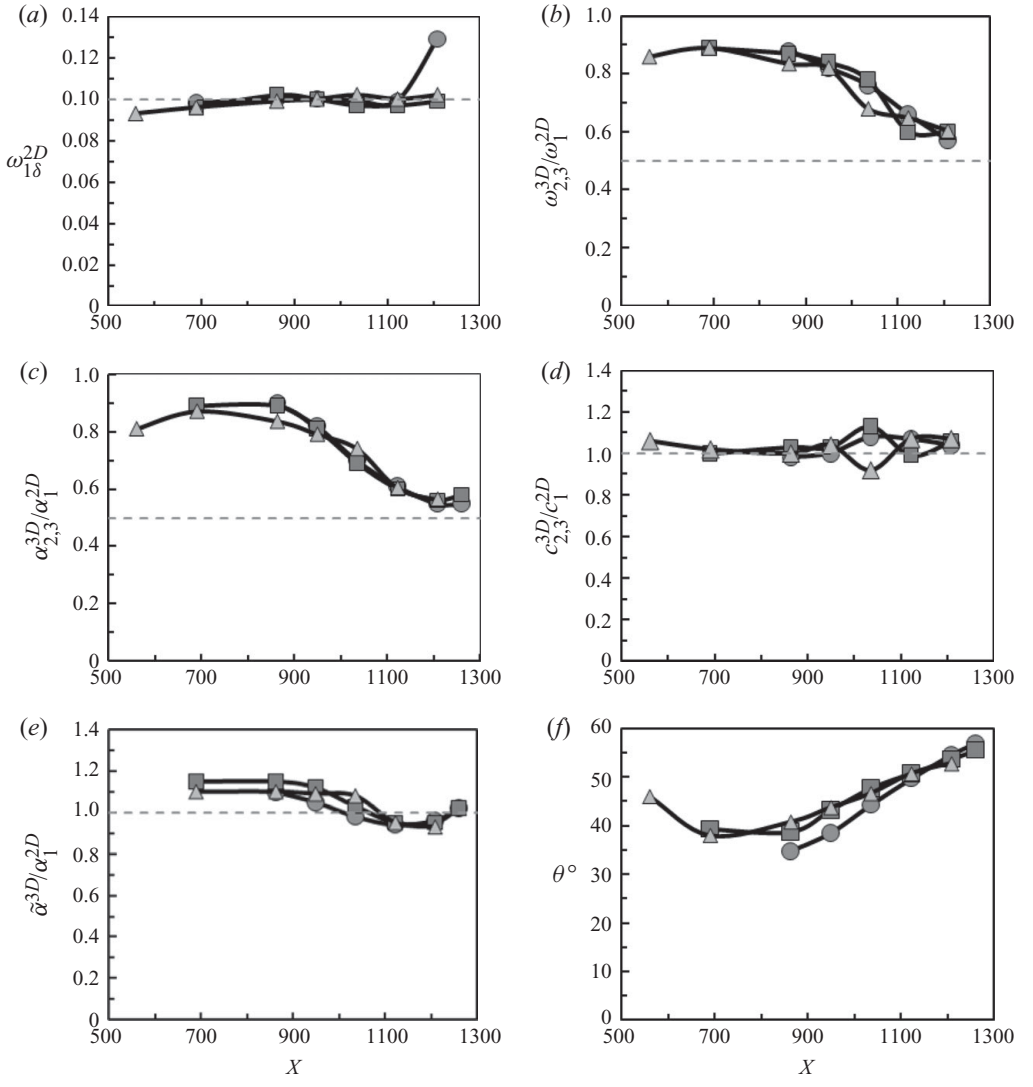

FIGURE 15. Spectral properties of dominant two-dimensional and three-dimensional wave modes given as a function of distance X: (*a*) $\omega_{1\delta}^{2D}$, (*b*) $\omega_{2,3}^{3D}/\omega_1^{2D}$, (*c*) $\alpha_{2,3}^{3D}/\alpha_1^{2D}$, (*d*) $c_{2,3}^{3D}/c_1^{2D}$, (*e*) $\tilde{\alpha}^{3D}/\alpha_1^{2D}$, (*f*) $\theta°$. Data are based on *u*-velocity fluctuations in the *u*-initiated wavepacket at $y/\delta \approx 0.62$, ●; *v*-initiated wavepacket at $y/\delta \approx 0.62$, ■; *v*-initiated wavepacket at $y/\delta \approx 1.2$, ▲.

late-to-post subharmonic stages at $X \approx 1260$. This indicates that the dominant phase-locked waves, subjected to wavenumber condition (3.3), are approaching a state of exact triad resonance (3.2). The latter case has been studied by Mankbadi, Wu & Lee (1993). The almost linear behaviour/growth of the fundamental two-dimensional waves through the subharmonic stage, as earlier observed in §§ 3.2–3.3, also appears to be consistent with its catalytic role in Wu *et al.*'s (2007) theory. The present results thus lend support to the theory proposed by Wu *et al.* (2007), and point to the possibility that phase locking is the generic and dominant mechanism for the nonlinear production of subharmonic waves in wavepackets in a Blasius boundary layer. The broadband growth of three-dimensional modes may also be seen in the

many spectral plots presented earlier, where the spectral peaks identify the dominant modes.

Subharmonic wave production has also been studied experimentally by Medeiros & Gaster (1999*b*) for wavepackets in a Blasius boundary layer. While probing further the mechanisms for subharmonic wave production, they found that the removal of Fourier wave components associated with the dominant subharmonic modes from their artificially synthesized initiating pulses had practically no effects on the subsequent production or emergence of subharmonic waves in the wavepackets. This holds for wavepackets with different initial phases. Medeiros & Gaster (1999*b*) inferred that the occurrence of the dominant subharmonic modes in the wavepackets might have proceeded from a deterministic cause that was not yet fully understood.

The typical pulse-excitation source generates a rich two-dimensional/three-dimensional wave spectrum. The continuity of c and $\tilde{\alpha}$ immediately implies that there is a neighbourhood of three-dimensional waves around any two-dimensional wave mode that could fulfil the weak matching requirements of Wu *et al.* (2007) for phase locking. The neighbourhood of three-dimensional waves could be quite large (to fairly large β) because, according to LST, the contours of c and $\tilde{\alpha}$ are roughly aligned in the same direction in the (α, β) plane at $\beta = 0$. This enhances the opportunity for approximate phase locking among two-dimensional and three-dimensional waves to occur, although the flow condition must also be right for approximate phase locking to drive the rapid growth of selected three-dimensional waves. Since three-dimensional waves are continually being produced through nonlinear wave interactions among existing waves, approximate phase locking provides a relatively accessible route for the growth of the three-dimensional spectrum. Nonlinear wave interactions and phase locking may thus work together to nurture the development of the three-dimensional spectrum, including promoting the growth of three-dimensional waves that may not even be present in the original spectrum at the time of source initiation. The present simulations show that the early subharmonic wave modes had evolved 'progressively' and 'contiguously' from the wave spectrum of the quasi-linear stage, instead of being a separate and distinct development. The early/incipient subharmonic modes are in fact quite close spectrally to the fundamental two-dimensional mode in terms of both frequency and streamwise wavenumber (figures 7*b* and 9*a*). The spectral proximity makes them potential candidates for approximate phase locking; indeed their $c_{2,3}^{3D}/c_1^{2D} \approx 1.0$ and $\tilde{\alpha}/\alpha_1^{2D} \approx 1.1$ at $X = 863$ and $y/\delta = 0.62$ in figure 15(*d*, *e*). The frequency and wavenumber ratios of the dominant three-dimensional/two-dimensional waves ($\omega_{2,3}^{3D}/\omega_1^{2D}$ and $\alpha_{2,3}^{3D}/\alpha_1^{2D}$ respectively) decrease from a high value of $\sim$0.9 (whilst adhering to the phase-lock conditions $c_{2,3}^{3D}/c_1^{2D} \approx \tilde{\alpha}/\alpha_1^{2D} \approx 1.0$) and approach the resonant value of 0.5 only in the late subharmonic stage (figure 15*b*, *c*). In this scenario, the presence of the dominant subharmonic frequency components in the initial source spectrum of the wavepackets may no longer be essential for those waves to subsequently emerge in the subharmonic stage – since they may apparently be derived through progressive evolution from a spectral neighbourhood of the dominant two-dimensional mode via phase locking. This may account for the persistent production of the dominant subharmonic waves in the experiments of Medeiros & Gaster (1999*b*), even though they had purposefully excluded those lower-frequency modes from the initial source spectra of the wavepackets. They had also observed that the fundamental and subharmonic spectral bands were not entirely separate in their experiments. Moreover, in Medeiros & Gaster (1999*b*) the wavepackets had evolved through a highly extended

linear stage – where it was likely that the lower-frequency components of the dominant subharmonic modes might even be initially suppressed had they been present. The spontaneous evolution of the dominant two-dimensional and oblique wave modes towards C-resonance (3.2) also suggests that such resonance may be an attractive state.

3.5. *Vortical structures in the evolving wavepackets*

In this section, we examine the vortical structures of the evolving u-initiated wavepacket. Figure 16(a) depicts the streamwise disturbance vorticity field ζ_x in a (y, z)-plane passing through the approximate centre ($X \approx 680$) of the wavepacket at time $T = 930$ in the quasi-linear stage. Because of the non-slip wall condition, the disturbance vorticity of the opposite signs is continuously being produced at the wall under the wavepacket. The ζ_x vortical system, comprising essentially two vortical stacks at this time, strengthens and expands sideway as the wavepacket convects forward. The sideway expansion of the ζ_x vortical system is driven by its interaction with the wall in the presence of the velocity gradient of the basic flow. The absence of a sustaining mechanism in the upper boundary layer, where the mean shear gradient tends to zero, limits the upward expansion of the ζ_x vortical system. At some point in the early subharmonic stage, a new vortical system emerges at the centre (see figure 16b), which is weak initially but grows quickly to rival the strength of the original vortical system outside. The most intense ζ_x vorticity belongs to the top central vortical pair, which is associated with the primary Λ-vortex. Corresponding spanwise vorticity (ζ_z) fields in the central plane ($z = 0$) are given in figure 17(a,b). Figures 16 and 17 have been plotted with a greatly magnified vertical scale to illustrate the developing vortices. If the vertical axis is correctly scaled relative to the horizontal scale, the organized vortices will compress into very thin vorticity sheets, with thickness-to-size ratio as small as 1/100. This shows that the evolving wavepacket physically comprises growing disturbance structures that are generated from the wall by viscosity in very thin overlapping vorticity sheets of alternating signs, arranged in stacks of two or three.

Vortex sheets are inherently unstable structures and have a tendency to roll up into vortical lumps under perturbation (Kelvin–Helmholtz-type instability). Some of the vorticity sheets in figure 16(c) exhibit vorticity concentrations that are suggestive of possible sheet instabilities. Evolving further downstream, the sheet vortices that develop in the central region are stretched by the large-amplitude low-frequency and low streamwise wavenumber u-velocity fluctuations (figure 3g) and the base flow as the wavepacket goes into the post-subharmonic phase. This results in the intensification of the ζ_x component of vorticity and the consequential roll-up of the vorticity sheet near the centre into streamwise-aligned vortices of small cross-section (see figure 16c). Mutual induction among these longitudinal vortices in the central region precedes the breakdown of the wavepacket into the incipient turbulent spot in figure 16(d), where a non-symmetric system of concentrated vortices (small cross-sections) may be seen. This region forms the core of the turbulent spot, while the outer vortex system (remnants of TS waves) continues to linger along the two sides of the turbulent spot as weak waves. Finally, figure 17(c) shows the high shear layer in the central plane formed at the post-subharmonic stage, which is then followed by wavepacket breakdown in figure 17(d).

Figure 18 shows the changing flow structures in the vicinity of the critical layer of the v-initiated wavepacket as it evolves from the quasi-linear stage to the early post-subharmonic stage. The streamtraces depict the total velocity field ($U + u - c$, $V + v$)

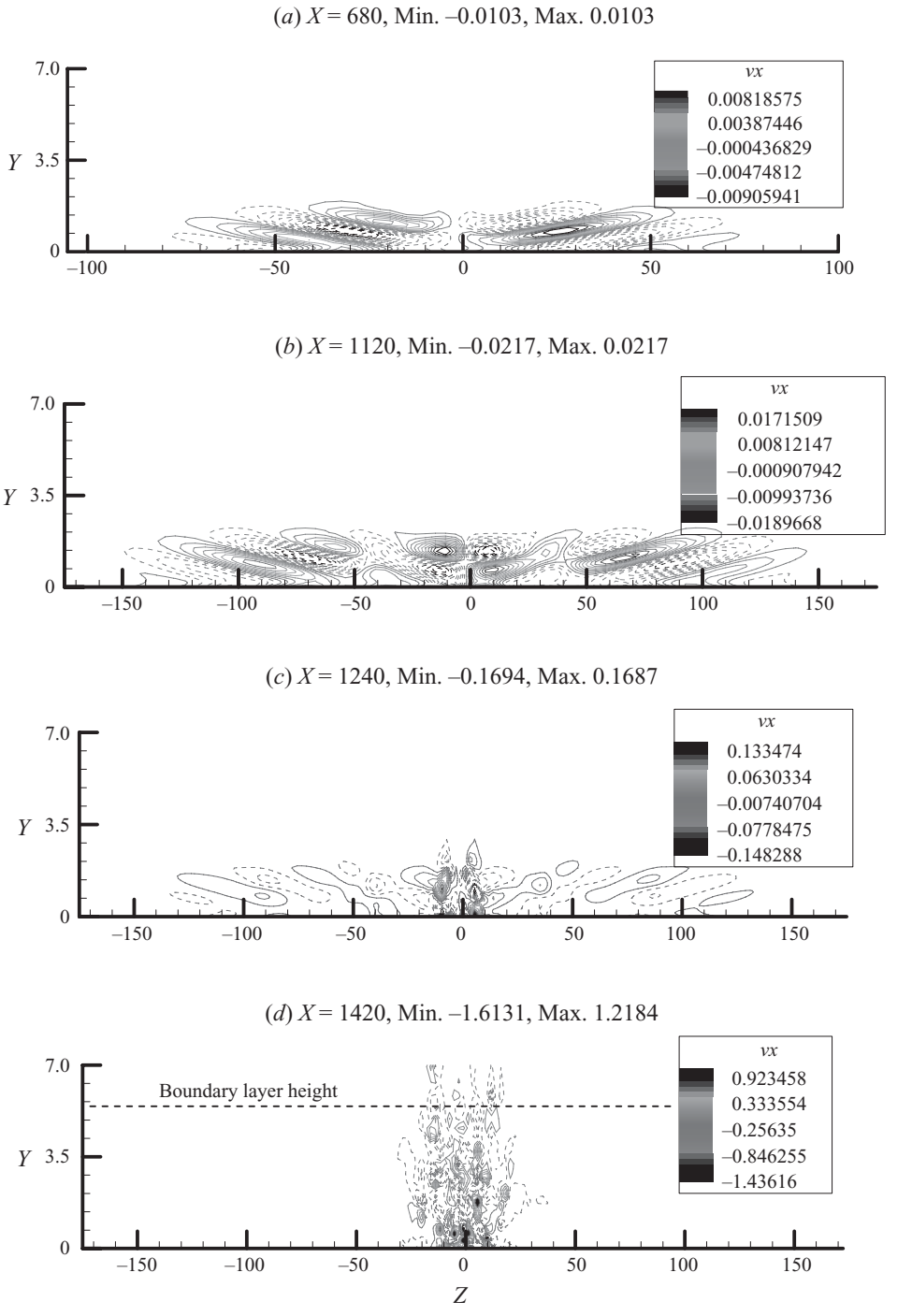

FIGURE 16. Contours of streamwise vorticity ζ_x at Y–Z plane passing through the approximate centre of the wavepacket: (*a*) $T = 930$; (*b*) $T = 1670$; (*c*) $T = 2417$; (*d*) $T = 2674$. Solid and dashed lines represent positive and negative contours, respectively. Minimum and maximum contour values are indicated (*u*-initiated wavepacket).

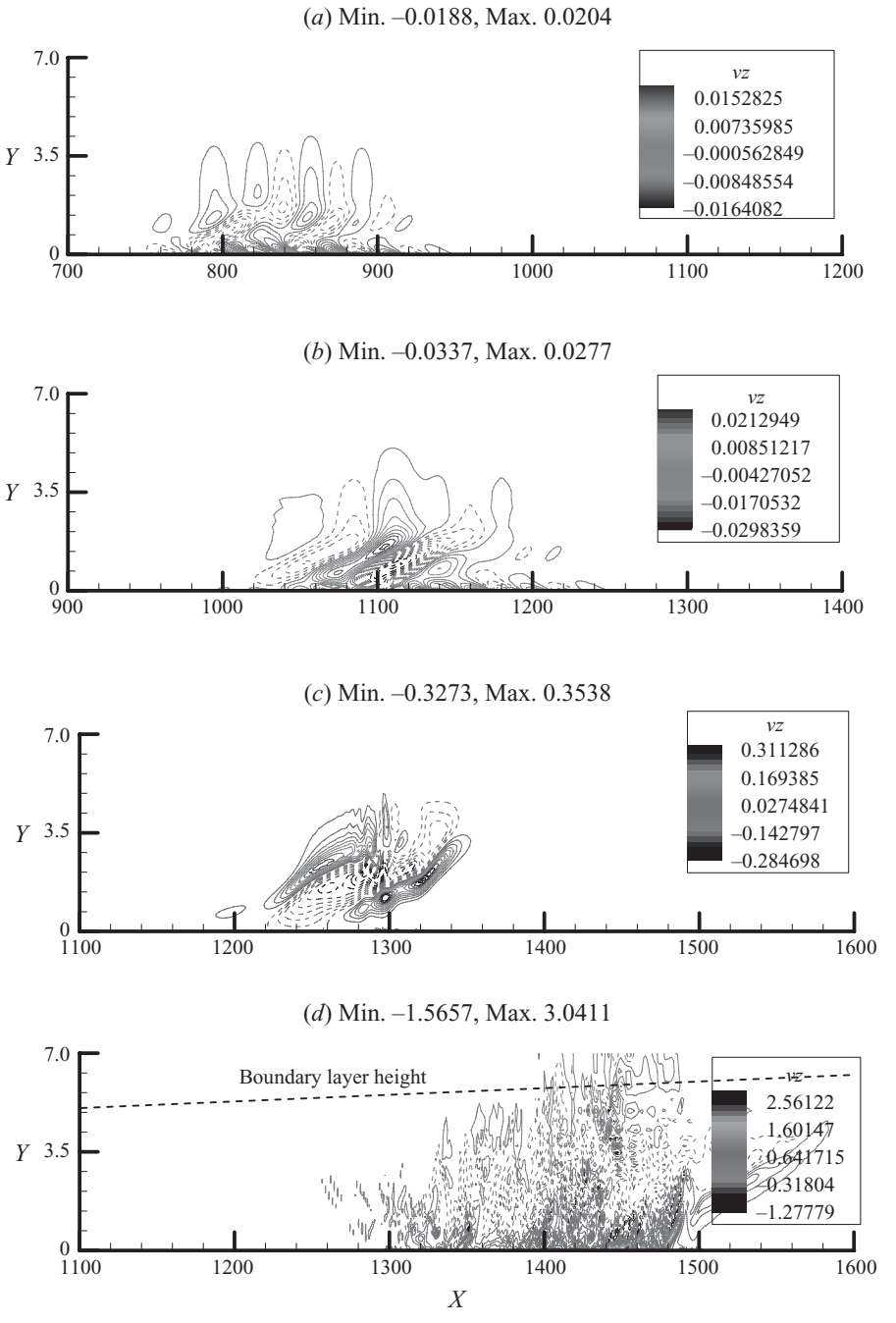

FIGURE 17. Contours of spanwise vorticity ζ_z along the centreline ($Z = 0$) of the wavepacket: (*a*) $T = 930$; (*b*) $T = 2046$; (*c*) $T = 2417$; (*d*) $T = 2674$. Solid and dashed lines represent positive and negative contours, respectively. Minimum and maximum contour values are indicated (*u*-initiated wavepacket).

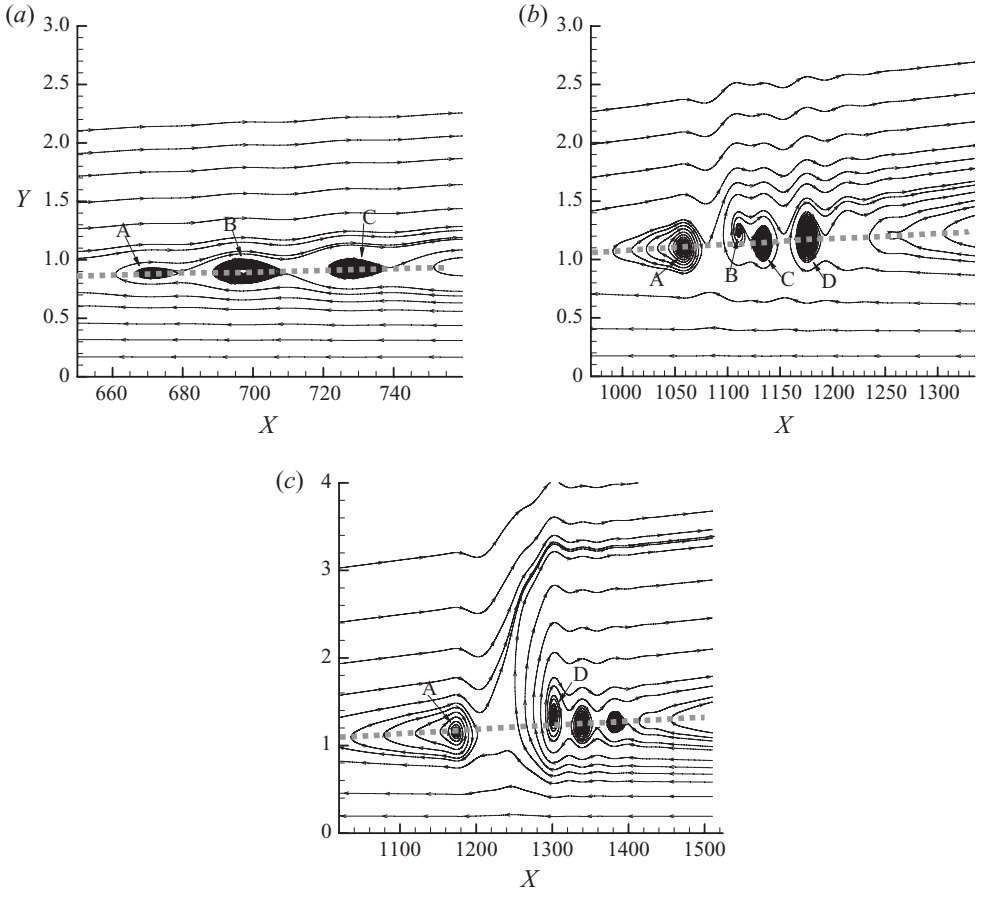

FIGURE 18. Streamtraces of velocity field $(U+u-c, V+v)$ at the central plane $Z=0$ at times: (*a*) $T=930$; (*b*) $T=2046$; and (*c*) $T=2418$ (v-initiated wavepacket). Wave speed $c=0.36$. Critical-layer height: ■■■■■■■■.

that would be seen by an observer travelling at the average wave speed ($c \approx 0.36$) of the dominant phase-locked waves. The velocity field of the linear wavepacket at $T=930$ in figure 18(*a*) reveals structures indicative of Kelvin's cat's eyes (see Drazin & Reid 1981). The closed streamlines usually associated with the cat's-eyes pattern are not present here because the base flow is slowly diverging and the disturbance is not exactly streamwise periodic. The propagation of the individual vortices (labelled by letters A–D) with time may be easily tracked from the convection speed and the elapsed time. Figure 18(*b*) shows the progressive coalescence of vortices B and C during the subharmonic stage, where the external field of vortex B may be seen to merge with the external field of vortex C to form streamtraces that encircle the cores of the two vortices. This process coincides with the formation of the primary Λ-vortex in the wavepacket. Their eventual coalescence results in the formation of a strong upward-directed jet (figure 18*c*) that transports/ejects lower-momentum fluid across the critical layer high up into the upper boundary layer in the post-subharmonic stage to form the well-known high shear layer in figure 17(*c*). The jet is clearly quite narrow spanwise according to figure 16(*c*), being generated between the two arms of the Λ-vortex (figure 3*g*).

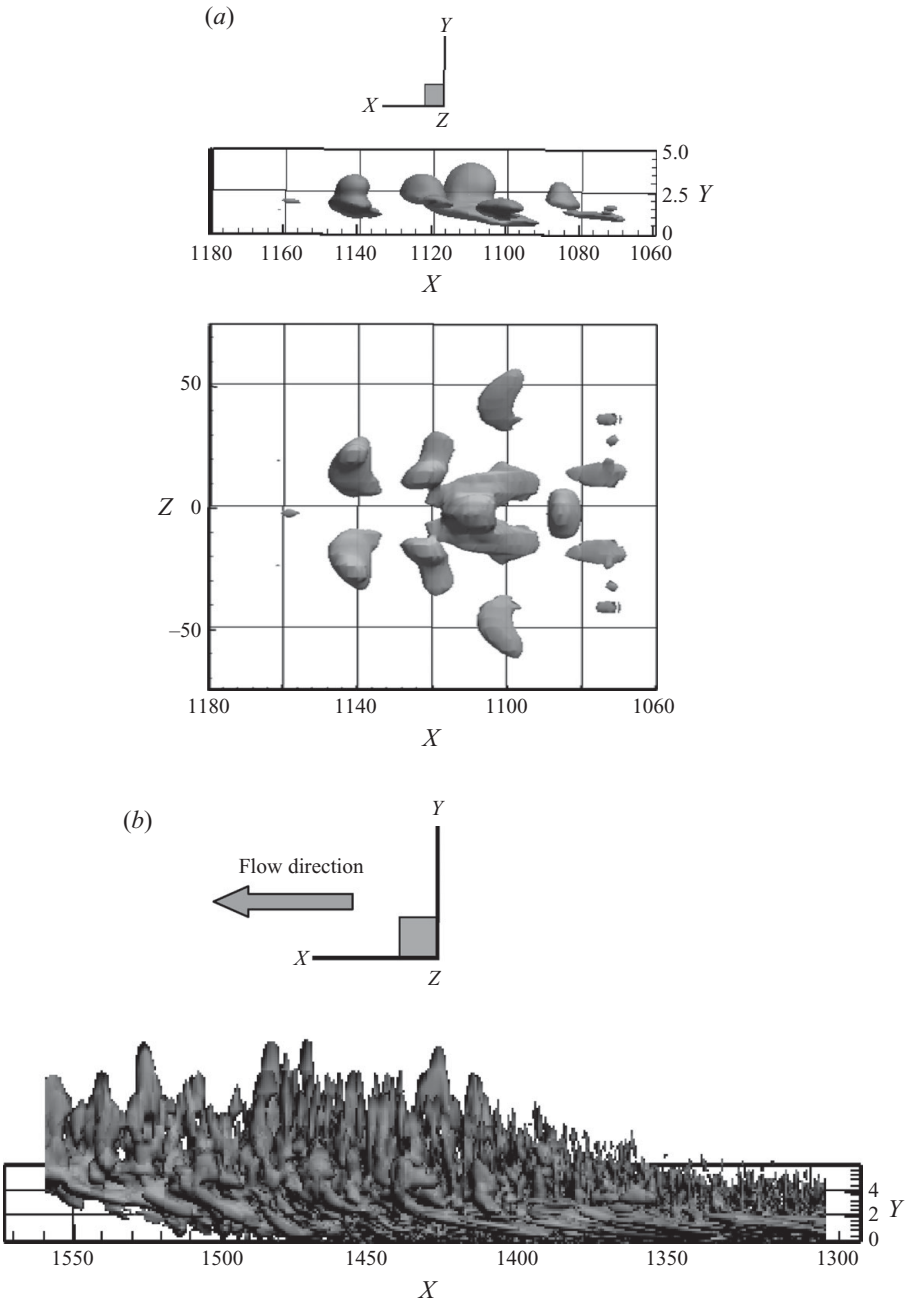

FIGURE 19. Vortical structures in u-initiated wavepacket: (a) side and plan views of Λ-vortex in the later subharmonic stage at $T = 2046$ ($\lambda_2 = -1.0 \times 10^{-6}$); ($b$) side view of incipient turbulent spot at $T = 2674$ ($\lambda_2 = -5.0 \times 10^{-6}$).

Figure 19(a) shows two views of the Λ-vortex in the later part of the subharmonic stage at time $T = 2046$, visualized in terms of vortical structures computed according to the $-\lambda_2$ criterion of Jeong & Hussain (1995). The vortical blob near the front of the Λ-vortex suggests strong self-induction that plausibly leads to pinching and

subsequent creation of ring vortex (see Moin *et al.* 1986; Rist *et al.* 1998). Finally, figure 19(*b*) shows the side view of the incipient turbulence spot at time $T = 2674$ as the amalgamation of a very large number of tube-like lifting/inclined vortical structures rising from the wall in the strong shear region of the boundary layer. The fore section of the spot comprises the larger-scale vortices with higher lifting rates, interspersed with smaller vortical formations. These vortices curve up sharply towards the vertical at the end of the incline to form a 'forest' of vortical blobs or puffs. The disturbance structures become increasingly fine towards the rear of the turbulent spot, where the spot thins down to a low mat of predominantly fine structures. The thinning down towards the rear may be explained in terms of the rapid decay of the vortices in the upper reaches of the boundary layer (where the mean shear gradient tends to zero) as the wavepacket convects forward, whereas vortical structures lower down in height decay more slowly due to interaction with the mean shear gradient of the near-wall flow.

4. Concluding summary

This study examines the evolution and breakdown of two pulse-initiated wavepackets (a *u*-velocity pulse and a *v*-velocity pulse) in a Blasius boundary layer via DNS. The basic flow parameters are modelled after the experiments of Cohen *et al.* (1991). The pulse-initiated wavepackets have a broad contiguous spectrum of two-dimensional and three-dimensional waves. The early growth of the wavepackets shows good overall agreement with the linear wavepacket theory of Gaster (1975). The three-dimensional spectrum extends contiguously to lower frequency and streamwise wavenumber as the wavepackets evolve into the subharmonic stage. The start of the subharmonic stage is marked by the emergence of a distinctive oblique wave pair with frequency $\omega_{2,3}^{3D} < \omega^{2D}$ (the subharmonic modes) within the developing three-dimensional spectrum. The incipient subharmonic modes are spectrally close in terms of their frequency and streamwise wavenumber to the fundamental two-dimensional mode. These have values that are substantially larger those anticipated for resonant–triad interaction (3.2). The subharmonic frequency $\omega_{2,3}^{3D}$ decreases towards the resonance value of $0.5\omega^{2D}$ as the dominant subharmonic and fundamental modes appear to evolve progressively towards resonance through the subharmonic stage. The dominant subharmonic oblique and fundamental two-dimensional waves have closely matching phase speeds ($c_{2,3}^{3D} \approx c_1^{2D}$) over much of the subharmonic growth stage, indicating that the growth of the subharmonic modes is governed by a critical-layer mechanism. The dominant subharmonic modes grow rapidly to dominate over the fundamental two-dimensional mode as the wavepacket evolves through the subharmonic stage.

The fundamental two-dimensional frequency remains nearly constant at $\omega_\delta^{2D} \approx 0.1$ over the linear and subharmonic stages. A comparison with LST shows that after an initial phase of growth, the dominant two-dimensional waves in the wavepackets evolve along the growth trajectory of the maximum linear amplification envelope. The dominant two-dimensional frequency $\omega_\delta^{2D} \approx 0.1$ observed in the present study and in the experiments of Medeiros & Gaster (1999*b*) is thus associated with the frequency of maximally amplified two-dimensional waves along the linear envelope in the applicable range of Re. A comparison with LST also shows that the lower-frequency waves in a band of spanwise wavenumbers about $\beta \approx 0.125$ ($\beta_\delta \approx 0.18$–$0.23$ for $R_\delta \approx 1500$–1900) begin to amplify nonlinearly, albeit weakly, quite early during the linear stage. The growth of the wavepacket is thus not fully linear even at a fairly

early stage. These waves become the most dominant waves in the wavepackets during the subharmonic stage. On the whole, velocity fluctuations within the wavepackets agree remarkably well with the eigenfunctions of LST even for the most amplified three-dimensional waves in the subharmonic stage.

The strongly nonlinear (post-subharmonic) stage is marked by interaction between the waves of the dominant oblique wave pair, resulting in the growth of near-zero and zero frequency longitudinal (streaky) structures at twice the spanwise wavenumber ($\pm 2\beta_{2,3}^{3D}$), strong distortion of the local base flow by the strengthening primary Λ-vortex and rapid expansion of the spanwise wavenumber (β) spectrum. This is a relatively brief stage compared to the preceding subharmonic stage. The final breakdown of the wavepacket, as indicated by rapid spectral expansion and loss of regularity in the wave structures, occurs within a short distance and time duration of about 5 % and 4 % of the total evolution distance and time from initiation, respectively. A large part of disturbance energy in the incipient turbulent spot is concentrated in a band of very low-frequency ($\omega \approx 0$), streamwise streaky ($\alpha \approx 0$) u-velocity fluctuations, which strongly distort the base flow under the turbulent spot. The v- and w-velocity fluctuations of the incipient turbulent spot contain relatively lesser energy, which are more evenly distributed across the higher harmonics of frequency and wavenumbers. The u- and v-initiated wavepackets evolve in broadly similar fashion and break down close to the same location. All key aspects of the present simulations have been corroborated by the experiments of Cohen *et al.* (1991), Breuer *et al.* (1997) and Medeiros & Gaster (1999*b*).

Rather than triad resonance, spectral data derived from the present simulations suggest that the subharmonic growth of wavepackets is governed primarily by the approximate matching of the phase speeds (c) and Squire wavenumbers ($\tilde{\alpha}$) of the dominant subharmonic and two-dimensional modes, in accordance with a recent phase-lock theory proposed by Wu *et al.* (2007). The agreement in c and $\tilde{\alpha}$ is largely within 10 % over the bulk of the subharmonic stage. The key feature of Wu *et al.*'s (2007) theory is that a two-dimensional planar mode may promote the rapid amplification of a broad spectrum of three-dimensional waves that share approximately the same phase speed as the two-dimensional mode. This is a significantly weaker condition than the triad resonance condition (3.2). The approximate phase-locking mechanism offers a relatively accessible route by which the three-dimensional wave spectrum could expand or regenerate. The present simulations show that the dominant oblique wave modes in the primary and late subharmonic stages originated from an incipient state/mode of substantially higher frequency in the spectral neighbourhood of the fundamental two-dimensional mode. This may explain why the dominant subharmonic waves invariably appeared in the experiments of Medeiros & Gaster (1999*b*), even though they had meticulously excluded the components of those waves from the source spectra of the wavepackets.

Finally, a visualization reveals that the evolving wavepacket comprises disturbance structures that are generated by viscosity from the wall in very thin overlapping sheets of vorticity of alternating signs, in stacks of two or three. Subharmonic instability begins with the formation of new vortical structures at the centre of the wavepacket. Streamwise stretching during the late and post-subharmonic stages promotes the roll-up and intensification of the vorticity sheets into dense longitudinal vortices in the central region. Their mutual induction or unstable interaction precedes the breakdown of the wavepackets. The creation and growth of the primary Λ-vortex is marked by the progressive coalescence of a pair of cat's-eye-like vortices at the critical layer. Their eventual coalescence leads to the formation of the well-known high-shear layer

in the post-subharmonic stage. The incipient turbulent spot is the amalgam of a very large number of streamwise-aligned lifting and raised vortices, which form an arrowhead-like structure pointing in the direction of the flow.

REFERENCES

Bech, K. H., Henningson, D. S. & Henkes, R. A. W. M. 1998 Linear and nonlinear development of localized disturbance in zero and adverse pressure gradient boundary layers. *Phys. Fluids* **10** (6), 1405–1418.

Borodulin, V. I., Kachanov, Y. S. & Koptsev, D. B. 2002*a* Experimental study of resonant interactions of instability waves in a self-similar boundary layer with an adverse pressure gradient. Part I. Tuned resonance. *J. Turbul.* **3** (62), 1–38.

Borodulin, V. I., Kachanov, Y. S., Koptsev, D. B. & Roschektayev, A. P. 2002*b* Experimental study of resonant interactions of instability waves in a self-similar boundary layer with an adverse pressure gradient. Part II. Detuned resonance. *J. Turbul.* **3** (63), 1–32.

Borodulin, V. I., Kachanov, Y. S. & Koptsev, D. B. 2002*c* Experimental study of resonant interactions of instability waves in a self-similar boundary layer with an adverse pressure gradient. Part III. Broadband disturbances. *J. Turbul.* **3** (64), 1–19.

Borodulin, V. I., Kachanov, Y. S. & Roschektayev, A. P. 2006 Turbulence production in an APG-boundary-layer transition induced by randomized perturbations. *J. Turbul.* **7** (8), 1–30.

Breuer, K. S., Cohen, J. & Haritonidis, J. H. 1997 The late stages of transition induced by a low-amplitude wavepacket in a laminar boundary layer. *J. Fluid Mech.* **340**, 395–411.

Cantwell, B., Coles, D. & Dimotakis, P. 1978 Structure and entrainment in the plane of symmetry of a turbulent spot. *J. Fluid Mech.* **87**, 641–672.

Cohen, J. 1994 The initial evolution of a wavepacket in a laminar boundary layer. *Phys. Fluids* **6** (3), 1133–1143.

Cohen, J., Breuer, K. S. & Haritonidis, J. H. 1991 On the evolution of a wave packet in a laminar boundary layer. *J. Fluid Mech.* **225**, 575–606.

Corke, T. C. & Mangano, R. A. 1989 Resonant growth of three-dimensional modes in transitioning Blasius boundary layers. *J. Fluid Mech.* **209**, 93–150.

Corke, T. C., Krull, J. D. & Ghassemi, M. 1992 Three-dimensional-mode resonance in far wakes. *J. Fluid Mech.* **239**, 99–132.

Craik, A. D. D. 1971 Nonlinear resonant instability in boundary layers. *J. Fluid Mech.* **50**, 393–413.

Crow, S. C. 1970 Stability theory for a pair of trailing vortices. *AIAA J.* **8**, 2172–2179.

Das, A. & Mathew, J. 2001 Direct numerical simulation of turbulent spots. *Comput. Fluids* **30**, 533–541.

Drazin, P. G. & Reid, W. H. 1981 *Hydrodynamic Stability*. Cambridge University Press.

Fasel, H. F. 1976 Investigation of the stability of boundary layers by a finite-difference model of the Navier–Stokes equations. *J. Fluid Mech.* **78**, 355–383.

Fasel, H. F., Rist, U. & Konzelmann, U. 1990 Numerical investigation of the three-dimensional development in boundary layer transition. *AIAA J.* **28** (1), 29.

Gaster, M. 1975 A theoretical model of a wave packet in the boundary layer on a flat plate. *Proc. R. Soc. Lond.* A **347**, 271–289.

Gaster, M. & Grant, I. 1975 An experimental investigation of the formation and development of a wavepacket in a laminar boundary layer. *Proc. R. Soc. Lond.* A **347**, 253–269.

Henningson, D. S. & Kim, J. 1991 On turbulent spots in plane Poiseuille flow. *J. Fluid Mech.* **228**, 183–205.

Henningson, D. S., Lundbladh, A. & Johansson, A. V. 1993 A mechanism for bypass transition from localized disturbances in wall-bounded shear flows. *J. Fluid Mech.* **250**, 169–207.

Henningson, D. S., Spalart, P. & Kim, J. 1987 Numerical simulation of turbulent spots in plane Poiseuille and boundary layer flows. *Phys. Fluids* **30**, 2914–2917.

Herbert, T. 1983 Subharmonic three-dimensional disturbances in unstable plane shear flow. *AIAA Paper* 83-1759.

Herbert, T. 1984 Analysis of the subharmonic route to transition in boundary layers. *AIAA Paper* 84-0009.

Herbert, T. 1988 Secondary instability of boundary layers. *Annu. Rev. Fluid Mech.* **20**, 487–526.

Holmes, P., Lumley, J. L. & Berkooz, G. 1996 *Turbulence, Coherent Structures, Dynamical Systems and Symmetry*. Cambridge University Press.

Jacobs, R. G. & Durbin, P. A. 2001 Simulations of bypass transition. *J. Fluid Mech.* **408**, 185–212.

Jeong, J. & Hussain, F. 1995 On the identification of a vortex. *J. Fluid Mech.* **285**, 69–94.

Kachanov, Y. S. 1994 Physical mechanisms of laminar–boundary-layer transition. *Annu. Rev. Fluid Mech.* **26**, 411–482.

Kachanov, Y. S. & Levchenko, V. Y. 1984 The resonant interaction of disturbances at laminar–turbulent transition in a boundary layer. *J. Fluid Mech.* **138**, 209–247.

Konzelmann, U. & Fasel, H. 1991 Numerical simulation of a three-dimensional wavepacket in a growing flat-plate boundary layer. In *Boundary Layer Transition and Control*, pp. 1–24. The Royal Aeronautical Society.

Liu, C. & Liu, Z. 1994 Multigrid mapping box relaxation for simulation of the whole process of transition in 3D boundary layer. *J. Comput. Phys.* **119**, 325–341.

Lundbaldh, A., Schmidt, P., Berlin, S. & Henningson, D. 1994 Simulations of bypass transition for spatially evolving disturbances. In *Application of Direct and Large Eddy Simulation to Transition and Turbulence. AGARD CP 551* (ed. B. Cantwell, J. Jimenez & S. Lekoudis), vol. 18, pp. 1–3.

Mankbadi, R. R., Wu, X. & Lee, S. S. 1993 A critical-layer analysis of the resonant triad in boundary-layer transition: nonlinear interactions. *J. Fluid Mech.* **256**, 85–106.

Medeiros, M. A. F. & Gaster, M. 1999*a* The influence of phase on the nonlinear evolution of wavepackets in boundary layers. *J. Fluid Mech.* **397**, 259–283.

Medeiros, M. A. F. & Gaster, M. 1999*b* The production of subharmonic waves in the nonlinear evolution of wavepackets in boundary layers. *J. Fluid Mech.* **399**, 301–318.

Moin, P., Leonard, A. & Kim, J. 1986 Evolution of a curved vortex filament into a vortex ring. *Phys Fluids.* **29**, 955–963.

Morkovin, M. V. 1969 The many faces of transition. In *Viscous Drag Reduction* (ed. C. Wells). Plenum.

Orszag, S. A. & Patera, A. T. 1983 Secondary instabilities of wall-bounded shear flows. *J. Fluid Mech.* **128**, 347–385.

Perry, A. E., Lim, T. T. & Teh, E. W. 1981 A visual study of turbulent spot. *J. Fluid Mech.* **104**, 387–405.

Reddy, S. C. & Henningson, D. S. 1993 Energy growth in viscous channel flows. *J. Fluid Mech.* **252**, 209–238.

Rist, U., Muller, K. & Wagner, S. 1998 Visualization of late-stage transitional structures in numerical data using vortex identification and feature extraction. Paper 103. In *Eighth International Symposium on Flow Visualization*, Sorrento, Italy.

Sartorius, D., Wuerz, W., Ries, T., Kloker, M., Wagner, S., Borodulin, V. I. & Kachanov, Y. S. 2006 Experimental study of resonant interactions of instability waves in an airfoil boundary layer. In *Sixth IUTAM Symposium on Laminar–Turbulent Transition. Fluid Mech. Appl.* **78**, 159–166.

Schmid, P. J. & Henningson, D. S. 2000 *Stability and Transition in Shear Flows*. Springer.

Shaikh, F. N. 1997 The generation of turbulent spots in a laminar boundary layer. *Eur. J. Mech.* B*: Fluids* **16**, 349–385.

Shaikh, F. N. & Gaster, M. 1994 The nonlinear evolution of modulated waves in a boundary layer. *J. Engng Math.* **28**, 55–71.

Singer, B. A. 1996 Characteristics of a young turbulent spot. *Phys. Fluids* **8** (2), 509–521.

Spalart, P. R. & Yang, K. S. 1987 Numerical study of ribbon-induced transition in Blasius flow. *J. Fluid Mech.* **178**, 345–365.

Vasudeva, B. R. 1967 Boundary-layer instability experiment with localized disturbance. *J. Fluid Mech.* **29** (4), 745–763.

Wang, Z. 2003 Computational simulation of unsteady boundary layer over compliant surfaces. PhD thesis, National University of Singapore.

Wang, Z., Yeo, K. S. & Khoo, B. C. 2005 Spatial direct numerical simulation of transitional boundary layer over compliant surfaces. *Comput. Fluids* **34**, 1062–1095.

Wang, Z., Yeo, K. S. & Khoo, B. C. 2006 DNS of low Reynolds number turbulent flows in dimpled channels. *J. Turbul.* **7** (37), 1–31.

White, F. M. 1991 *Viscous Fluid Flow*, 2nd edn. McGraw-Hill.

Williamson, C. H. K. & Prasad, A. 1993*a* A new mechanism for oblique wave resonance in 'natural' far wake. *J. Fluid Mech.* **256**, 269–313.

Williamson, C. H. K. & Prasad, A. 1993*b* Acoustic forcing of oblique wave resonance in the far wake. *J. Fluid Mech.* **256**, 315–341.

Wu, X. & Stewart, P. A. 1996 Interaction of phase-locked modes: a new mechanism for rapid growth of three-dimensional disturbances. *J. Fluid Mech.* **316**, 335–372.

Wu, X., Stewart, P. A. & Cowley, S. J. 2007 On the catalytic role of the phase-locked interaction of Tollmien–Schlichting waves in boundary-layer transition. *J. Fluid Mech.* **590**, 265–294.

Wygnanski, I., Sokolov, M. & Friedman, D. 1976 On a turbulent spot in a laminar boundary layer. *J. Fluid Mech.* **78**, 785–819.

Zhao, X. 2007 Computational simulation of wavepacket evolution over compliant surfaces. PhD thesis, National University of Singapore.